

Modeling ribosome dwell times and relationships with tRNA loading and codon usage in mammals

Gobet Cédric^{1,2}, Weger Benjamin^{1,2}, Marquis Julien^{2,3}, Martin Eva², Gachon Frederic^{*1,2,4}, Naef
Felix^{*1}

¹ Institute of Bioengineering, School of Life Sciences, Ecole Polytechnique Fédérale de Lausanne, Lausanne CH-1015,
Switzerland

² Nestlé Research, CH-1015 Lausanne, Switzerland

³ Current address: Lausanne Genomic Technologies Facility, Université de Lausanne, Lausanne CH-1015, Switzerland

⁴ Current address: Institute for Molecular Bioscience, The University of Queensland, St. Lucia, Brisbane, QLD 4072,
Australia

★ Corresponding authors

Abstract

Protein translation depends on mRNA-specific initiation, elongation and termination rates. While the regulation of ribosome elongation is well studied in bacteria and yeast, less is known in higher eukaryotes. Here, we combined ribosome and tRNA profiling to investigate the relations between ribosome elongation rates, (aminoacyl-) tRNA levels and codon usage in mammals. We modeled codon-specific ribosome dwell times and translation fluxes from ribosome profiling, considering pair-interactions between ribosome sites. In mouse liver, the model revealed site and codon specific dwell times, as well as codon pair-interactions clustering by amino acids. While translation fluxes varied significantly across diurnal time and feeding regimen, codon dwell times were highly stable, and conserved in human. Fasting had no effect on codon dwell times in mouse liver. Profiling of total and aminoacyl-tRNAs revealed highly heterogeneous levels that correlated with codon usage and showed specific isoacceptor patterns. tRNAs for several amino acids were lowly loaded, which was conserved

in fasted mice. Finally, codons with low levels of charged tRNAs and high codon usage relative to tRNA abundance exhibited long dwell times. Together, these analyses pave the way towards understanding the complex interactions between tRNA loading, codon usage and ribosome dwell times in mammals.

Introduction

Translation regulation dynamically controls gene expression in processes such as development, the cell cycle, circadian rhythms, and response to nutrients [1]. At least three steps underlie protein translation: translation initiation, often thought to be rate limiting, elongation, and termination[2]. Recently, however, elongation has emerged as an important layer to fine-tune gene expression (reviewed in [3]). Indeed, variations in elongation rates may influence mRNA stability [4, 5, 6], nascent protein folding [7], and even feedback on the initiation rates [8]. For example, recent studies showed that alteration of ribosome elongation rates in cancer cells influences their proliferation and invasion capabilities [9, 10, 11].

While the links between translation elongation and gene expression are increasingly studied, the mechanisms influencing ribosome elongation rates are poorly understood, notably in higher eukaryotes. In unicellular organisms, codon-specific elongation rates are well explained by cognate tRNA concentrations [12]. This is also reflected evolutionary, since highly expressed genes are enriched for fast codons with high concentrations of tRNAs and favorable codon-anticodon interactions [13]. However, this concept has been challenged since pioneering work in *E.coli* showed that ribosomes move at different speeds on the codons GAA and GAG [14]. These codons are decoded by the same tRNA, raising the possibility that elongation rate is not only determined by the concentration of tRNAs.

More recently, the development of ribosome profiling (RP) shed new light on the regulation of translation elongation and revealed supplementary layers of complexity [15]. Indeed, the possibility to capture the positions of translating ribosomes on mRNAs [16] provided genome-wide

insights on key features regulating ribosome speed. For instance, the properties of amino acids [17], (aminoacyl-) tRNA availability [18, 19, 20], tRNA modifications [21, 22, 23], secondary structures of mRNAs [24, 25], folding of the nascent chain [26], pairs of codons [27, 28], and sterical interactions with the ribosome exit tunnel [29] were shown to influence the local density of ribosomes on transcripts. While RP studies have brought new knowledge on translation elongation, these were performed mostly in unicellular organisms and have led to divergent results as highlighted in several meta-analyses [30, 31]. One reason is that ribosome footprints are sensitive to biases from differences in protocols [32, 33], drug usage [34, 35, 36], library preparations [37], and data analysis pipelines. Consequently, the reported correlations between ribosome dwell times (DTs), tRNA abundances, and codon usage frequency and bias [38] showed inconsistencies. In addition, while codon usage can be precisely estimated, it is difficult to measure tRNA concentrations. Indeed, tRNAs exhibit a high degree of modifications and complex secondary structures, which alter cDNA synthesis and biases quantification by high-throughput sequencing [39]. Even less is known about tRNA loading levels. Thus, direct measurements of tRNA levels are typically lacking. Finally, further layers of complexity involve factors such as the Translation elongation factor P (EFP) in bacteria, and the homolog Translation initiation factor 5A (eIF5A) in eukaryotic cells. These factors regulate translation elongation by resolving stalled ribosomes on sequences with inefficient peptide bond formation. Through the stabilization of amino acid (AA) pairs via their hypusinated residue, these factors increase the efficiency of peptide bond formation [40] at sequences such as polyproline [41], glycine (Gly), or positively charged AA [42, 43].

Thus, to better establish the determinants of ribosome elongation in higher eukaryotes, we here combined modeling of RP data, codon usage analysis, and (aminoacyl-) tRNA profiling in mouse liver. Notably, to understand the dependencies of AA supplies on (aminoacyl-) tRNA and ribosome elongation rates, we performed experiments on mice fed *ad libitum* (AL) or in fasted (FA) conditions. We developed a statistical model to capture the influence of codons, AA, and

ribosome site interactions on RP densities along transcripts genome-wide. In yeast, our analysis confirmed previously measured slow inter-site codon pairs. In mouse liver, we found a wider range of codon- and AA-specific ribosome DTs, and inter-site codon pairs involving mainly the ribosome P and A sites. Meta-analysis in mammals revealed a conserved translational landscape, and highlighted technical biases in RP signals, as confirmed using new RP experiments in AL fed and FA mice. Finally, we extended a recent tRNA profiling method [9] to quantify (aminoacyl-) tRNA levels in liver of AL and FA mice. With those tRNA levels and codon usage properties, we were able to explain some codon-specificity in ribosome DTs.

Results

Modeling ribosome fluxes and codon-specific DT including ribosome inter-site interactions

RP counts along transcripts typically show large variations with high and low densities of ribosomes (Fig.1C). When the density of ribosomes per transcript is low (no traffic jams), the probability of finding a ribosome at a specific position on an mRNA is proportional to the translation initiation rate times ribosome DTs (Fig.1A). Further assuming steady-state and no ribosome drop-off, the translation flux per mRNA (number of ribosomes passing at a given position on the mRNA per unit of time) is constant along transcripts and equal to the initiation rate per transcript, as regulated typically by 5'- untranslated regions (UTRs) [44]. The total translation flux is then equal to the translation flux per mRNA multiplied by the number of mRNAs. As introduced, ribosome DTs depend on the codons translated in the E, P, and A sites, as well as surrounding sequences (Fig.1A). To determine the DTs, we developed a generalized linear model (GLM) for the observed RP read counts genome-wide, which models the expected read counts as gene specific fluxes (gene covariates) multiplied by ribosome DTs (codon covariates), and uses appropriate noise models (Methods). The same model is also applied on RNA-seq experiments

(when available) to normalize the fluxes per mRNA, and attenuate possible technical biases. We modeled DTs additively (in log) using site-specific contributions of the three E, P, and A sites and their surrounding codons, as well as possible pair interactions between the E, P, and A sites, noted E:P, P:A, or E:A. (Fig.1A-B). The GLM used the 61 sense codon alphabet, and we considered positions around the ribosome spanning 120 nucleotides around the E site (Fig.1B). Unlike previous algorithms [30, 31, 25], we developed a bioinformatics pipeline allowing to fit globally, for each condition, all model parameters (DTs and gene specific fluxes) from the reads counts at every position on the coding sequences (CDSs) (Fig.S1A-C) (Methods). Our model faithfully captured raw RP signals along genes, including high peaks and valleys in read density (Fig.1C).

In yeast ribosome DTs anti-correlate with codon usage and display inter-site interactions

To validate our model, we analyzed two published RP datasets in *Saccharomyces cerevisiae* [20, 45]. One set was under normal (WT) [45] conditions and one treated with 3-amino-1,2,4-triazol (3-AT), which inhibits the histidine (His) biosynthesis pathway [20] thereby reducing loaded His-tRNAs. Both datasets used cycloheximide (CHX) only in the lysis buffer. Codon-specific DTs in WT exhibited about a four-fold range at each of the three E, P, and A sites (Fig. 2A-B, left). While codons for proline (Pro) and arginine (Arg) showed long DTs in all three sites, and were longest in the P site, codon for isoleucine (Ile), leucine (Leu), and valine (Val) were fastest in the A site (Fig. 2A-B, left).

As expected, we found that the shortage of His in the 3-AT condition resulted in increased DTs in the P and A sites for both His codons (CAC and CAT) (Fig. 2A-B, right). Interestingly, outside the E,P,A sites, DTs showed a dependency on His codons at around 30 nucleotides (positions 11 and 12) downstream of the P-site (Fig. S2A), likely reflecting queued ribosomes (disomes) behind His codons[20]. Also, some Arg codons showed slightly increased DTs in the upstream

sequence, highlighting possible interactions of this positively charged AA with the ribosome exit tunnel (Fig. S2A).

Moreover, the DTs also displayed signatures of technical biases. Notably, the high variation in DTs at position -4, coinciding with the most 5' nucleotide of the insert, was previously shown to reflect a bias in library preparation (Fig. S2A) [37]. To further validate the biological relevance of our DTs, we compared ribosome DTs in WT condition with codon usage weighted (wCU) by mRNA translation levels, to take into account condition-specific demands in codons. Interestingly, we found high negative correlations ($R^2 = 0.565$ and $R^2 = 0.495$) between the wCU and the DTs at the P and A sites (Fig. 2C). This observation suggests an evolutionary pressure to enrich for fast codons in highly expressed genes, and conversely.

In addition to the site-specific DTs, we probed whether pairs of codons in the ribosome sites synergize by adding E:P, P:A, and E:A interaction terms to the modelled DTs (Fig. S2B-D). We compared these predicted DTs with a GFP-reporter experiment in yeast probing for pairs of codons inhibiting translation[28]. Indeed, the experimentally determined inhibitory pairs (EDIPs) exhibited long predicted DTs at the E-P and P-A sites (Fig. 2D). While for these pairs the summed DTs from the individual sites were already long, the interaction terms clearly improved the match (Fig. 2E-F). Interestingly, though the E:P and P:A interactions were not correlated overall, EDIPs showed similarly strong DT contributions from E:P and P:A (Fig. 2G). Globally these interaction matrices were sparse and not highly structured, but revealed large values and spread for the pairs involving codons for Arg or Pro (Fig S2B-D). Moreover, the total DTs for the 61^2 codon pairs (including the single sites and interactions summed for the E-P and P-A sites) revealed Arg in most of the top 50 slowest pairs, making this AA potent at decreasing translation elongation rate. Conversely, Val was contained in most of the fastest pairs. Thus, modeling RP data can identify subtle properties of ribosome DTs, such as codon-specific and inter-site contributions, signatures of sequences outside of the E, P, and A sites, and library biases.

Site-specific and inter-site codon DTs (for A and P sites) in mouse liver cluster by AA

Since much less is known in mammals, we applied this model to our previous RP study aimed at analyzing translation levels during feeding fasting cycle in mouse liver (84 samples). These data used WT and circadian clock deficient mice subjected to 12h-12h light-dark cycles, and livers were harvested at different Zeitgeber times (ZT, with ZT0: lights on, ZT12: lights off) around the 24 h day. While gene-specific translation fluxes varied over time and between genotypes, DTs were remarkably stable and showed high correlations between the samples (Fig. S3A-B). Therefore, for the following analyses, we averaged the DTs over all the 84 samples. Global patterns of DTs for the E, P, and A sites showed striking differences with yeast, and notably exhibited a larger dynamic range (Fig. 3A-B). In fact, the P and A sites revealed nearly 10-fold change between the fastest and slowest codons, while the E site had a tighter DT distribution (Fig. 3A-B). While DTs in the P and A site were overall more strongly correlated to each other than with the E site, DTs also showed clear site-specificity. For instance, the four codons for Gly had long DTs in the P site, however, the Gly GGT codon was among the fastest in the E and A sites, while the GGA codon was markedly slow in the A site. Also, all three Ile codons had long DTs in the A site but a very short DT in the P site (Fig. 3A-B). For the negatively charged glutamate (Glu) and aspartate (Asp), all their codons showed long DTs in the P and A sites (Fig. 3A-B). Considering a larger window around the ribosome revealed that P and A sites, followed by the E site, contributed the largest effects (Fig. S4A). Upstream and downstream sequences outside the (-4,+6) interval did not contribute (Fig. S4A), while codons in the vicinity of the ribosome (-3, -2, -1 and +3, +4, +5) exhibited significant and correlated variations in DTs on both sides. The detected signals at the -4 and +6 positions likely reflect ligation biases during the library preparation. Inter-site codon pair DTs revealed a significantly influence on translation elongation in mouse liver, with P:A interactions showing the widest dynamic range, followed by E:P and E:A (Fig. S4D). Note that the interaction matrices are

not symmetric, showing codons or AA specificity at the respective ribosome sites. Intriguingly, the P:A interaction matrix highlighted a striking clustering by amino acid (AA) for the A site (Fig. 3C), while E:P interactions clustered by AA in the P site (Fig. S4B). This suggests that inter-site DTs are determined by AAs and their influence on the peptide bond formation. The clustering by AA was corroborated by a model selection analysis on the 84 samples, where the alphabet for the DT regression coefficients was taken as either the 20 natural AA, or the 61 sense codons (Fig. S4C). While the preferred alphabet was overall that of the codons, the model with AA coefficients at the A site for the P:A interaction was preferred to all the other models (Fig. S4C). In the case of the E:P interaction, the AA alphabet in the P site was considered as the best model. Overall, models including the site interactions were preferred to the reduced models, emphasizing the importance of inter-site interactions in determining ribosome DTs in mouse liver. In fact, the codon-pair interactions contributed to the total DTs in the P and A site by a factor larger than 2 for about one hundred pairs (Fig. 3E). The P:A matrix revealed strong positive interactions (ones lengthening the DTs) for pairs of bulky AAs (Pro, tryptophan (Trp) and phenylalanine (Phe)) or achiral (Gly) (Fig. 3C and E). As in yeast, Arg codons were part of the slowest pairs (Fig. 3C and E). Surprisingly, the known stalling pair (Pro-Pro) showed the largest negative interaction (Fig. 3C and E), possibly related to eIF5A activity. The E:P matrix was more complex: pairs involving the AA Gly, Asp, Asparagine (Asn), and Pro in the P site lengthened the total E-P pair DTs (Fig. S4B). Unlike in yeast (Fig. 2C), ribosome DTs did not correlate with wCU in mouse liver (Fig. 3D). On the gene level, there was no signature of a link between mean DTs and translation levels (flux), arguing against an evolutionary selection of CDSs based on translation elongation times. Nevertheless, genes containing slow codons (long mean DTs) were enriched for biological functions related to the cytoskeleton (Fig. S4E). Together, our models of RP data revealed a rich translation elongation landscape in mammalian tissues.

Ribosome DTs in liver are conserved under fasting

The above analysis showed highly robust DTs between liver samples collected during the normal feeding (night) fasting (day) cycle (Figure S3A-B). To probe whether ribosome DTs are sensitive to longer periods of fasting and a subsequent decrease in AA, we performed new RP experiments in mice fed either ad libitum (AL) or fasted (FA) (Fig. 4A). Since DTs can be sensitive to RP protocols, we here used a small RNA-Seq protocol with random adapters to reduce possible ligation biases and PCR duplicates. Moreover, as ribosome dynamics and DTs are affected if CHX is added to the growth medium in yeast [34, 46], we tested conditions without CHX in the lysis buffer.

First, we investigated the effect of prolonged fasting (up to 30 hours) by analyzing differential RP signals between AL and FA. Genes related to the Peroxisome Proliferator-Activated Receptor α (PPAR α) pathway and to fatty acids oxidation were upregulated in FA, presumably to provide the energy needs (Fig. 4D). On the contrary, genes related to lipid biosynthesis were downregulated in FA (Fig. 4D), suggesting that animals switched from glucose to fatty acid metabolism in FA, as already described [47]. Moreover, *Mat1a*, *Asl* and *Got1* related to AA biosynthesis were upregulated in FA (Fig. 4D), further validating the fasted state of the mice. The RP data in the new conditions showed a typical tri-repeat nucleotide pattern (Fig. 4B and S5B), confirming the presence of *bona fide* translating ribosomes in the FA samples, as well as in samples without CHX (NOCHX). Looking into the codon DTs, AL and FA mice highlighted surprisingly conserved patterns (Figs. 4C and S5C) in both the CHX or NOCHX conditions, including the inter-site codon DTs (Fig. S5D). Moreover, these DTs were highly correlated with those from the 84 samples (Fig. S6C-D). Nevertheless the FA samples showed a reduced dynamic range, presumably due to variability in RP signal quality. Finally, we probed whether possible differences in codon usage could counterbalance the presumed shortage of AA in FA. Strikingly, when considering the wCU bias in WT and FA animals, we found that most of the codons with a G or C nucleotide at the third position (GC3) were enriched in up-regulated transcripts in

228 FA, while codons with an A or T nucleotide were underrepresented (Fig. S5E).

229 **Meta-analysis of RP data sets reveals conserved DTs in mammals**

230 To further investigate these highly stable DTs, we analyzed other published RP datasets in
 231 mouse liver (H: Howard *et al.*) [48], mouse kidney (CS: Castelo-Szekely *et al.*) [49] and human
 232 liver cell line Huh7 (L: Lintner *et al.*) [50]. In the CS and L data, RP libraries were prepared
 233 using circularization methods and the monosome-protected fragments were retrieved using size-
 234 exclusion chromatography or sucrose cushion. In the H data, RP libraries were prepared as in
 235 our case with a small RNA-seq protocol that uses adapter ligation, and monosome-protected
 236 RNA fragments were retrieved through a sucrose gradient. Codon DTs at the A site were highly
 237 correlated between the mammalian datasets ($0.48 < r < 0.96$), including in different tissues
 238 (kidney) and human cells (Fig. S6C, E). However, the mammalian DTs were markedly different
 239 from those in yeast. In addition to the clearly dominant contribution of the P and A sites, sub-
 240 stantial variation in estimated DTs was found around positions -4 and +6, probably reflecting
 241 library preparation biases. In contrast, ours and the H samples (Fig. S6A-B) showed highly
 242 enriched DTs at the P and A sites (Fig. S6A-B), presumably reflecting ribosome dynamics
 243 more faithfully. Moreover, the inter-site codon pair DTs (P:A) were also more consistent across
 244 experiments with that protocol (Fig. S6D). Together, this meta-analysis confirmed the repro-
 245 ducibility of modelled DTs; moreover, it uncovered biases in RP library preparation leading to
 246 modified RP signals near read extremities, and reducing the signals in the A and P sites for
 247 some protocols.

248 **(Aminoacyl-) tRNA profiles are conserved in fed and fasted mice**

249 We next asked whether the estimated DTs can be linked with tRNA abundances or loading levels,
 250 which is poorly studied in higher eukaryotes [38]. The chemical modifications and secondary
 251 structure of tRNAs render them difficult to quantify. A recent hybridization method [9] combined

with sequencing allows to bypass the problematic cDNA synthesis step to quantify tRNA levels.

To measure tRNA abundances and assess possible links with ribosome DT, we adapted and optimized this method to target all annotated mouse tRNAs (Fig. S7A). Moreover, we quantified the fraction of (aminoacyl-) tRNAs using sodium periodate [51], which depletes unloaded tRNAs by selective biotinylation of 3'-ends (Fig. S7A). This way, we aimed to quantify the tRNA pools available for elongation in the ribosome A site. tRNA molecules are encoded by a large number of genes. Therefore, we designed 303 DNA probe pairs (left and right) to target all mouse tRNA sequences from the *GtRNAdb* database (Table S3). Our modified protocol yielded a high proportion of specific ligations between left and right probes, showing target specificity for tRNAs (Fig. S7B). Indeed, mapping of the sequencing reads to all possible combinations (303^2) of left and right probes showed that more than 75% of ligated products belonged to tRNA genes of the same codon (Fig. S7B), and even 95% were from probe pairs that could be assigned to specific codons with high confidence (Fig. S7B) (Method). Further experiments validated the specificity and evaluated the efficiency of DNA ligases (Fig. S7C-D).

We performed tRNA profiling on mouse livers from the same samples as those used for the RP. Specifically, we quantified the total tRNA (control, NaCl) abundances and the (aminoacyl-) tRNAs (periodate, NaIO₄) from the same pieces of liver in two replicates in the AL and FA conditions, at three different time points (ZT04, ZT12, ZT18) (Fig. 5A, Methods). tRNA abundances for the NaCl/AL condition exhibited a large dynamic range (Fig. 5B). Interestingly, tRNA levels for AA encoded by four synonymous codons ("4-codon" box) stood out. Indeed, these were highly expressed and represented by one dominant isoacceptor with a T at the wobble position 34 (*e.g.* TGC/Ala, TGG/Pro, TCC/Gly, TAC/Val, TGT/Thr) (Fig. 5C). The three other tRNA isoacceptors were very lowly expressed. Comparison of these tRNA abundances with PolIII ChIP-Seq in mouse liver [52] revealed a significant correlation (Fig. S7E).

The distributions of tRNAs in the different samples were well conserved and showed only small variations over the biological conditions, except for mitochondrial tRNAs (Fig. S7G). Strikingly

though, principal component analysis (PCA) on the four conditions (*i.e* NaCl/AL, NaCl/FA, NaIO₄/AL and NaIO₄/FA) exhibited a clear separation between the control and periodate conditions (Fig. 5D), indicating differential loading of the tRNAs. Surprisingly, the AL and FA samples were indistinguishable in the total tRNA and (aminoacyl-) tRNA conditions (Fig. 5D-E), indicating no imbalance of tRNA charging in FA. However, some codons for Asn, Asp, Ile, and Arg were lowly aminoacylated (by nearly 10-fold), independently of the feeding regime (Figs. 5E, S7F).

Relationship between (aminoacyl-) tRNA levels, codon usage, and DT

Finally, we investigated whether variations of codon DTs and wCU could be explained by the available tRNA pools. In lower organisms, it is known that codon usage frequency and tRNA pools co-adapted to fine-tune translation elongation. However, whether this relation holds in mammals is debated, mainly due to the lack of good proxy for tRNA levels. Moreover, codon usage differences seem to be driven by mutational bias such as GC content [53]. Here, we discovered a significant correlation between wCU and our directly measured tRNA levels in mouse liver (Fig. 6A), extending previous works using POLIII loadings on tRNA genes as proxies [53]. Our analysis also highlighted codons with high or low demand (codon usage) compared to the supply (tRNA levels), as quantified by the codon balance[54].

DTs in the A site did not exhibit a simple correlation with tRNA abundances (Fig. 6B), nor with the codon balance (Fig. 6C), highlighting more complex translation elongation regulation. However, some codons clearly stood out; in particular, the slow DTs for Glu codons (Fig. 3A) may well result from their low codon balance, hence limiting tRNA availability at the A site. Similarly, while DTs in the A site were overall poorly correlated with tRNA aminoacylation levels, codons for Asp, Asn, and Ile, which had particularly lowly charged tRNAs, coincided with some of the slowest DTs (Fig. 6D). We therefore included several effects in a linear model, which uncovered that a linear combination of tRNA aminoacylation levels and codon balance

captures a significant portion of variation in the A site DTs, particularly the long DTs for Glu, Asp, Asn, and Ile codons (Fig. 6E).

Discussion

We extensively modeled RP data and uncovered codon-specific and inter-site DTs determining ribosome elongation rate in mammals. These DTs were highly stable across all conditions tested. In parallel, we quantified (aminoacyl-) tRNA levels in mouse liver and identified several features regulating ribosome elongation, such as aminoacylation levels and tRNA/codon usage balance. In yeast, our model accurately inferred codon-specific DTs and highlighted mainly Arg and Pro as slow in the A and P sites. These AAs are known for their inefficient peptide formation and sterical interactions with the ribosome [41, 55]. A significant negative correlation was observed between DTs and wCU, probably reflecting natural selection for fast codons in highly translated genes. While this relationship has been described [56, 31], the found correlation is, to our knowledge, the highest reported. Moreover, our analysis confirmed recently identified inhibitory pairs (EDIPs) [28], and deciphered their synergistic effect in addition to the site-specific contributions. We showed that the EDIPs had slow DTs both on the E:P and P:A positions, highlighting potentially inefficient translocation of the pair due to wobble base-pairing or other mechanisms [28]. In mouse liver, DTs differed significantly from yeast, showing a larger spread and higher complexity. Remarkably, DTs were conserved between different tissues and RP protocols. Moreover, the DTs were consistent with a pausing motif described in mouse embryonic stem cells (mESCs) [57].

We found that the smallest and achiral AA Gly exhibited very long DTs (in the A and P site) that differed between all isoacceptors and tissues (*i.e.* liver and kidney). Interestingly, in bacteria, Gly codons are slow, although this effect is still difficult to separate from Shine-Dalgarno (SD) dependent stalling [58] or protocol artifacts [59] and is therefore debated [60]. As mam-

328 mals do not use a SD mechanism, our result support an alternative hypothesis, such as slow
329 codon-anticodon pairing [61] or inefficient peptide bond formation. Pioneering work in *E. coli*
330 suggested that Gly-tRNAs adopt a particular conformation due to the U nucleotide in position
331 32 and that unmodified U_{34} on $tRNA_{UCC}^{Gly}$ could decode the four Gly codons (a pairing known
332 as superwobbling [62]), but with low efficiency (reviewed in [61]). While this mechanism was
333 shown in unicellular organisms, our tRNA profiling found $tRNA_{UCC}^{Gly}$ as the major Gly isoac-
334 ceptors and one of the most abundant tRNAs in mouse liver, supporting this hypothesis. The
335 DTs for the acidic AAs (Asp and Glu) were among the slowest. Glu showed a particularly
336 low balance of tRNA levels/codon usage and Asp tRNA was lowly charged. This could lead
337 to a shortage of tRNA availability and therefore ribosome stalling. As their codons share the
338 same first two bases, competition with near-cognate tRNAs [22], or pairing inefficiency due to
339 the wobble mechanism could also explain the long DTs. Indeed, slower elongation would allow
340 higher precision in codon-anticodon discrimination [63]. Ile codon DTs were slow in the A site
341 while fast in the P site. Remarkably, the isomeric leucine codons were the fastest in the P and A
342 sites, highlighting a structure independent mechanism. Indeed, we showed that Ile-tRNAs were
343 lowly aminoacylated, reducing Ile availability on the A site, but other explanations are possible.
344 For instance, since Ile is decoded by three different codons, a suitable pairing mechanism such
345 as inosine or other U_{34} modifications could be used to avoid pairing of the fourth near-cognate
346 codon (Met) and therefore increase the DTs [64].

347 One of our main results concerned the contributions of codon-pair interactions between ribosome
348 sites towards DTs, mainly at the P and A site. At these positions, the ribosome catalyzes the
349 peptide bond formation between (aminoacyl-) tRNA in the A site and peptide-tRNA bound to
350 the P site. Our analysis revealed that the identity of the AA in the A site (acceptor), and not
351 the codon, was the best descriptor of those codon pair interactions. Pairs including bulky AAs
352 or Gly in the A site were slow, highlighting their potential inefficiency in peptide bond forma-
353 tion. Interestingly the DT for Pro-Pro pairs, known to inefficiently form peptide bonds [65],

was markedly reduced by the interaction. This observation probably shows the role of eIF5A in resolving this stalling motif. On the other hand, Gly, Asp, and Glu, which were slow in our analysis, were shown by others to require eIF5A for their efficient translation [43, 42]. These AAs are known to be enriched in stalled ribosomes in eIF5A-depleted cells [42] and in proteins related to cytoskeleton and migration-associated behavior [66, 67]. Interestingly, we showed that proteins related to cytoskeleton such as collagens have a relatively long mean elongation times. Liver diseases such as fibrosis or hepatocellular carcinoma exhibit upregulated eIF5A, making this protein a potential target for treatment or prognosis in these diseases [68, 66].

Other features not included in the model, and which are independent of the codon identity, might regulate ribosome elongation. A high number of liver proteins are secreted and thereby translated by ribosomes bound to the endoplasmic reticulum (ER) via the interaction of signal recognition particles with the nascent peptide chain. These interactions are known to stall the ribosomes, however, as these appears to be codon independent, we did not detect them in our analysis [25]. In addition, chaperone proteins interacting with the nascent peptide were shown to influence co-translational folding and subsequent ribosome density on mRNAs [69]. RNA secondary structure and modifications as well as pseudo-knots acting as ribosome roadblocks, and slippery sequences inducing frame shifting, could extend the parameter space of our model [25, 70, 71, 72].

While we found a striking correlation between DTs and wCU in yeast, the same did not hold in mammals. This suggests that biased codon usage in mammals reflects more complex evolutionary forces, such as mutation driven GC bias[53]. Nevertheless, the measured tRNA abundances showed signatures of adaptation, since tRNA levels correlated with the wCU. These correlations extended previous results at the transcription level or in highly expressed genes [53, 73]. Related to this, one still open challenge is to assign tRNAs to their corresponding codons, due to the extended wobble base pairing rules related to tRNA modifications.

Surprisingly, tRNA loading was unaffected by prolonged fasting. Several studies in cell lines

showed that decreasing AAs in culture media leads to a decrease in (aminoacyl-) tRNA availability and therefore increases ribosome stalling [51, 18]. Moreover, others have shown that codon optimality contributes to differential mRNA translation in response to starvation [19]. While we did not observe this, probably due to the *in vivo* state, GC3 bias (*i.e.* GC bias at position N3 in codons) was significantly different between genes translated in AL and FA mice or also between night and day conditions (not shown). Genes with high GC3 content have been shown to provide more targets for methylation than those with low GC3 and to be enriched in stress responsive genes [74]. Nevertheless, the reason of the higher GC3 level in FA compared to AL still need to be identified.

Like (aminoacyl-) tRNA levels, DTs were unchanged between AL and FA. We can hypothesize that after more than 30 hours of starvation, mice are compensating the lack of AAs by a large global decrease of translation initiation through mTORC1/GCN2 [75], making tRNA availability and translation elongation non limiting. Moreover, since RP signals, DTs and tRNAs were measured in relative and not absolute amounts, we cannot exclude a total decrease of translation elongation rate, aminoacylation or tRNA levels.

In conclusion, ribosome DTs, codon usage, tRNA levels, and translation elongation in mammals do not seem to obey simple relationships. Nevertheless, although a global understanding is still missing, we were able to link both tRNA/codon usage balance and aminoacylation levels with anomalously slow DTs in the P and A site of the ribosome. Probing different ribosome states (*e.g.* free A site) using RP combined with different drugs [59] or improving the quantification of (aminoacyl-) tRNA through nucleotide modification removal [76] will lead to better understanding of the determinants of translation elongation. Finally, more work is needed to understand the consequences of changes in ribosome elongation rates for mRNA stability and nascent protein folding.

Methods

Inference of DT and translation fluxes

Preprocessing of RP data

RP from yeast, mouse and human were respectively mapped on the sacCer3, mm10 and Hg38 genomes using STAR [77] with parameters `-seedSearchStartLmax 15`. Genomes indexes were built using Ensembl transcripts annotations. Adapters were retrieved for the different datasets and input as parameter for STAR. In the case of NEXTFlex library, fastqs files were parsed and duplicated sequences (UMI and insert) are removed. Sequences were trimmed for adapters using `fastx_clipper` with parameters `-Q33 -a TGG AATTCTCGGGTGCCAAGG -l 11` and UMIs are removed (4 nucleotides on both sides) . Then, the fastq files are mapped using STAR with options `-seedSearchStartLmax 15`. The subsequence BAM files were sorted and indexed.

Read counting on the CDSs

For each protein coding transcript with a CDS larger than 120 nucleotides, reads with zero mismatches, unique mapping (`nM:i:0 & NH:i:1`) and a length between 25 and 40 nucleotides were retrieved using `samtools view` in the respective region. E site position was defined for each read. From this position, the sequence in the window `[-60,+60]` nts was reported and incremented by one at each new observation. Sequences with a window spanning the start or stop codon were removed.

Filtering

A sliding window of 120 nucleotides moving 3 by 3 on the CDS of protein coding genes were computed and the respective sequences were reported (Figure S1A). This set of sequences is used as a reference and their respective number of counts is set to zero. Every time a read occurs at one of these sequences, we incremented the count by one (Fig.S1B) . Genes with less than 5%

of positions covered or less than 5 positions observed were discarded. Genes with less than 100 counts were removed. Sequences containing a stop codon (TAG, TGA or TAA) or non-unique in the genome were discarded. Depending on the sample coverage, we monitored about 5000 genes in mammals.

Generalized linear model

We used a generalized linear model for the observed RP read counts at the different positions on the gene CDS. The read counts at a specific codon position i corresponding to the ribosome E site on the CDS of a gene g in sample s were modeled as a negative binomial with mean μ_{igs} and dispersion parameter θ_s . θ_s was taken as a sample specific parameter and was empirically estimated using pairs of codons occurring more than once on a gene. For those pairs of codon, the respective mean and variance of counts were computed and θ_s were inferred globally by linear regression using Eq.1.

$$\begin{aligned} Y_{ig} &\sim NB(\mu_{ig}, \theta) \\ E[Y_{ig}] &= \mu_{ig} \\ \text{Var}(Y) &= \mu + \frac{\mu^2}{\theta} \end{aligned} \tag{1}$$

The model for each sample is as follows (we omitted the sample index for clarity) :

$$\begin{aligned} h(\mu_{i,j}) &= \underbrace{f_g}_{\text{gene}} + \left(\sum_{k=-20}^{20} \underbrace{\tau_{k,c(i+k)}^{(1)}}_{\text{single}} \right) + \underbrace{\tau_{c(i+s1),c(i+s2)}^{(2)}}_{\text{pairs}} + \text{offset}(\text{library size} + \text{RNA-Seq}) \\ \text{with}(s_1, s_2) &\in \begin{cases} (0, 1) \text{ for the E:P fit} \\ (0, 2) \text{ for the E:A fit} \\ (1, 2) \text{ for the P:A fit} \end{cases} \end{aligned} \tag{2}$$

where the offset term makes the gene fluxes normalized by library size and expressed per mRNA,
and $c(i) \in \{AAA, AAC, AAG, \dots, TTT\}$. $h(x) = \log(x)$ the natural link function for count data.
 $\tau_{k,c(k)}^{(1)}$ the individual codon DT for the 61 sense codons in log scale at position k , with k the
relative position to the ribosome E site. $\tau_{c(i+s1),c(i+s2)}^{(2)}$ the inter-site codon pair DT for the 61^2
pairs of sense codons in log scale at positions (s_1, s_2) relative to the ribosome E site. These
codon pairs are modeled for the sites E:A, E:P, and P:A. f_g the gene flux in log scale.
The fit was performed using *glm4()* function from the R package *MatrixModels* with the noise
family *negative.binomial*(θ_s) from the *MASS* package and with sparse design matrix option.
Sequencing library size is used as an offset. RNA-Seq data is fitted (when available) and read
counts are predicted at every positions and used as an offset.
Since this problem does not have full rank, we set for the fit : $\tau_{k,AAA}^{(1)} = 0$ for $\forall k$ and $\tau_{(AAA,.)}^{(2)} = 0$,
 $\tau_{(.,AAA)}^{(2)} = 0$, $\tau_{(AAT,AAT)}^{(2)} = 0$. To present the results, we then chose the more natural convention
(zero average): $\sum_c \tau_{k,c}^{(1)} = 0$ for all k , $\sum_c \tau_{c,c'}^{(2)} = 0$ for all c' , and $\sum_{c'} \tau_{c,c'}^{(2)} = 0$ for all c and shifted
the gene fluxes accordingly.

Differential expression in AL vs. FA

Two outlier samples (ZT12/FA/CHX and ZT04/FA/NOCHX) were excluded for the differential
expression analysis and DT modelling . Statistics were computed using EdgeR [78] comparing
a model including factors for time, feeding, and drug conditions against a model without the
feeding term.

Animals experiments

Animal studies were approved by the local ethics committee, and all protocols were approved
by the Service Vétérinaire Cantonal (Lausanne, Switzerland) under license VD3613. 8 weeks
old male C57BL6/J mice (Charles River Laboratory) are kept under diurnal lighting conditions
(12-h light, 12-h dark) at a temperature of $21^\circ\text{C} \pm 2^\circ\text{C}$. After a complete night of fasting,

the mice were kept without access to food for an additional period of up to 24 hours. During this time period animals were sacrificed every 8 hours starting at ZT4. Control animals were kept on *ad libitum* feeding regimen.

Ribosome profiling

Samples preparation for RP was performed as described in [79] except for the conditions without cycloheximide (CHX) in which fresh livers were directly lysed in ice-cold lysis buffer without CHX and directly flash-frozen in liquid nitrogen. To limit possible bias due to footprint size selection related to different conformations of the ribosome [58] [33], a larger band was cut on the TBE-gel. Libraries were generated using NEXTflex Small RNA Sequencing Kit v3 (bioo scientific) following the manufacturer's protocol. Samples were pooled based on the Illumina indices used. Denaturated pools were spiked with 5% PhiX and clustered (loading equivalent to 3 samples per lane) onto a rapid single-end v2 flowcells at a concentration of 8pM. Libraries were sequenced on a HiSeq 2500 (Illumina) for 50 cycles.

(Aminoacyl-) tRNA profiling

The tRNA profiling protocol was adapted and modified from [9]. We tested the initial protocol [9] on mouse liver samples but the results showed a high proportion of unspecific ligations between the left and right probes from distinct tRNAs. We solved this issue by inverting the order of two steps in the protocol: we performed the pull-down and cleaning on magnetic beads before the splint ligation between the two DNA probes on the tRNA (Fig. S7A) Oxidation of 3'-tRNA by periodate was adapted from [51]. All the steps were performed under cold and acidic conditions to avoid deacylation of the tRNAs before Na periodate oxidation.

Probe Design

DNA probes were designed to target all the annotated mouse tRNAs from <http://gtrnadb.ucsc.edu/>. The database contains tRNA gene predictions by tRNAscan-SE [80]. tRNA se-

quences for *Mus musculus* (GRCm38/mm10) were downloaded and spliced *in silico*. The sequences were split in the middle of the anticodon in order to design left and right probes. After reverse complementation of the sequences, overhangs (for PCR primer binding) and unique molecular identifiers (UMIs, 2x6N) were added (right-probe adapter:

5'-GCACCCGAGAATTCCANNNNNTGG-3, left-probe adapter:

5'-NNNNNNGATCGTCGGACTGTAGAACTC-3'). Left probes were ordered with a 5'-phosphate to allow ligation with the right probe upon annealing with the corresponding tRNA. The random nucleotides were ordered as «high fidelity wobble» to ensure homogeneous representation of the four bases in the UMI and to avoid bias. DNA probes were ordered at MicroSynth AG (Switzerland).

tRNA extraction and oxidation

50-100 μ g of frozen mouse liver tissues were weighted under cold conditions. Beating beads were added and the samples were homogenized in 350 μ l of cold Qiazol (Qiagen) lysis reagent in a TissueLyser (Qiagen) for 2 x 2 min at 20 Hz. Tubes were left 5 min at room temperature. 140 μ l of CHCl₃ was added and homogenates were shaken vigorously followed by centrifugation at 4°C for 15 min (12'000 x g). The upper aqueous phase was carefully removed and 1 volume (350 μ l) of buffered phenol (Phenol:chloroform:isoamyl alcohol, 25:24:1, pH 4.9) was added. Samples were mixed and centrifuged for 15 minutes at 4°C (12'000 x g). Upper phase (300 μ l) was supplemented with 1 volume (300 μ l) of cold isopropanol, precipitated 30 minutes at 4°C and then centrifuged for 15 minutes at 4°C (12'000 x g). RNA pellets were dried at room temperature and re-suspended in 500 μ l of Sodium Acetate buffer pH 4.9 (0.2M). Samples were split in two tubes (2 x 250 μ l) for sodium periodate oxidation (NaIO₄) or control (NaCl) treatment. 50 μ l of NaCl (0.3M) or NaIO₄ (0.3M) was added and samples were incubated for 30 minutes at room temperature. The reaction was then supplemented with 300 μ l Ethanol (70%) and loaded on a miRNeasy column (Qiagen). tRNA were extracted following the miRNA easy protocol from

Qiagen. 390 μ l Ethanol (100%) was added to the flow through and loaded on a MinElute column (Qiagen). Columns were washed following the manufacturer's protocol and RNAs were eluted in 15 μ l RNase-free H_2O .

Deacylation

Purified tRNAs (14 μ l) supplemented with 6 μ l of Tris-HCl (pH 8) were deacylated by heating at 40°C for 35 minutes. Reaction was stopped by the addition of 30 μ l NaAcetate (0.3 M). RNAs were purified using RNA Clean & Concentrator -5 kit (Zymo) according to manufacturer's instructions and eluted in 15 μ l RNase-free H_2O .

3'-tRNAs biotinylation

3'-tRNAs biotinylation was adapted from Pierce RNA 3'-End Biotinylation Kit (Thermo Fisher). Deacylated tRNAs were denatured in 25% DMSO at 85°C for 5 minutes and directly chilled on ice. Biotinylation was performed in a 90 μ l reaction with 6 U of T4 ssRNA Ligase (NEB), 4 μ l Biotinylated Cytidine (Thermo Fisher, 1mM), 2 U RNase inhibitor, 9 μ l RNase Buffer (NEB), 9 μ l ATP (NEB, 10m M), 40 μ l PEG 800 (50%) and 20 μ l denatured RNAs. The reaction was performed overnight at 16°C. Biotinylated tRNAs were cleaned using RNA Clean & Concentrator -5 kit (Zymo) according to manufacturer's instructions and eluted in 20 μ l H_2O .

Probes hybridization

DNA probes were synthesized by *Microsynth AG* and resuspended at a 100 μ M concentration. The 606 probes were then mixed at an equimolar ratio (0.15 μ M each) and aliquoted for further usage. Hybridization of probes was performed in a 300 μ l-reaction with 45 μ l probes mastermix, 30 μ l hybridization buffer 5x (EGTA, NaCl, Tris-HCl), 205 μ l RNase-free water and 20 μ l tRNAs. After a 15 minutes denaturation at 95 °C (in a PCR cycler), the mixture was slowly cooled down to 55 °C (0.2 °C/second) and incubated for 30 minutes.

Beads purification

200 μ l of Dynabeads MyOne Streptavidin C1 (Thermo Fisher) were washed following manufacturer's instructions for RNA usage. 250 μ l of beads, re-suspended in washing buffer (2x), were incubated with 300ul of the resulting RNA-DNA hybridization reaction for 40 minutes with gentle rotation. Beads were washed/magnetized three times with 1ml of washing buffer (1x) and re-suspended in 300 μ l H_2O .

RNA-DNA hybrid ligation

Bead purified DNA-RNA hybrid on beads were ligated at the anticodon nick by a combination of SplintR and T4 DNA ligases (NEB) to minimize ligation efficiency bias. 300 μ l of DNA-RNA hybrids were splint-ligated with 2.5 U of SplintR DNA ligase and 30 μ l of SplintR DNA ligase buffer (10X, NEB) for 1 hours at 25 °C. Then, 10 U of T4 DNA ligase (NEB) and 33 μ l of T4 DNA ligase buffer (10x, NEB) were added. Ligation was performed overnight at 16 °C.

RNA digestion

Beads were magnetized and washed once with washing buffer (1X) to remove any remaining ligases. Next, beads were re-suspended in 10 μ l H_2O . 2 U of RNase A (Thermo Fisher) and 10 U of RNase H (NEB) with RNase H buffer (10X) (NEB) were added and digestion was performed for 30 minutes at 37 °C . Elution buffer (5X) was added for a final concentration of 50 mM tris pH8, 10 mM EDTA, 1% SDS was added and samples were incubated at 65 °C for 30 minutes with intermittent shaking to retrieve ligated DNA probes. Beads were magnetized and supernatant extracted. DNA ligated probes were purified using DNA Clean & Concentrator -5 kit (Zymo) according to manufacturer's instructions and eluted in 20 μ l RNase-free H_2O .

qPCR for quality control and relative concentration estimation

The relative concentration of the resulting DNA ligated-probes was assessed by quantitative PCR (qPCR) using the LightCycler 480 SYBR Green I Master kit (Roche). 3.5 μ l of $\frac{1}{10}$ diluted samples was used to assemble a 10 μ l reaction and run on a Light Cycler 480 II (Roche) with the primers CAGAGTTCTACAGTCCGACGAT and TTGGCACCCGAGAATTCCA (matching each probe's ends) at a final concentration of 0.3 μ M. Cycling conditions consisted of an initial denaturation step of 5 min at 95 °C followed by 40 cycles of 30 s at 95 °C and 45 sat 45 °C. The C_p obtained were used to calculate the optimal number of PCR cycles amplification required for library amplification, as described previously [79]. The number of required cycles were between 13 and 17 depending on the experiments and samples. The quality of the ligation was assessed on a Bioanalyzer small RNA chip (Agilent Technologies).

PCR amplification

The PCR was designed following Illumina's recommendation taking advantage of the indexed oligos from the TruSeq small RNA kit. A 50 μ l-reaction was assembled with Kapa Polymerase and 15 μ l of DNA ligated probes, and run for the optimal number of PCR cycles calculated as described above.

Library postprocessing

Amplified libraries were purified with 100 μ l AMPure XP beads (Beckman) and eluted in 20 μ l resuspension buffer (10 mM Tris, pH8.0). Libraries were quantified with Picogreen (Life Technology) and usually yield 50-400 ng DNA. The libraries size patterns were checked using a fragment analyzer (Agilent).

Library Sequencing

An equimolar library pool was prepared from the individual libraries based on the concentrations calculated from Picogreen data. Pools were denaturated with NaOH and neutralized with HT1 buffer (Illumina) to reach a final concentration of 20pM. Pools were spiked with 10 % PhiX and clustered (loading equivalent to 12 samples per lane) onto a rapid single-end flow cell v2 at a final concentration of 7pM. Sequencing was performed on a HiSeq 2500 (Illumina) in rapid mode for 130 cycles.

Data Analysis

To assess the fidelity of left/right probe ligation and efficiency of hybridization, a fasta file with all the possible combinations between left and right probes was created. In case two tRNA genes share the same left/right probes, they were grouped and annotated accordingly. It led us to a total of 68526 sequences. Genome index was generated with STAR with options

`-runMode genomeGenerate -genomeSAindexNbases 3`. Fastq files were trimmed for adapters. Sequencing reads were aligned against the index with parameters:

```
-outFilterScoreMinOverLread 0 -outFilterMatchNminOverLread 0
-winAnchorMultimapNmax 1000 -outFilterMismatchNmax
-clip3pNbases 6 -clip5pNbases 6
-outFilterMultimapNmax 50 -outSAMattributes NM nM NH NM -alignIntronMax 1
-alignEndsType EndToEnd -seedSearchStartLmax 20 -seedMultimapNmax 100000.
```

For each combination, the number of counts were computed and corrected for PCR duplicates using both unique molecular identifiers sequences. Reads larger than 60 nucleotides with less than 3 mismatches and less than 5 insertions compared to the reference were retained. Combinations with less than 10 reads were discarded. Reads mapping to combinations of probes coming

from different codons were reassigned in function of the newly ligated sequence. Abundances of tRNA coding for the same codon were summed up and normalized by library size using *edgeR* R package [78]. Because tRNA moieties (the two halves of the tRNA) have very similar sequences, and since the specificity of the hybrid DNA-RNA around the anticodon is important for the ligation, we used the sequence around the anticodon to reassign the ambiguous combinations.

Data Availability

Sequencing data of this study have been submitted to Gene Expression Omnibus (GEO) under accession number GSE126384: <https://www.ncbi.nlm.nih.gov/geo/query/acc.cgi?acc=GSE126384>. Datasets and GEO references: Atger Liver (all 84 RP samples, GSE73553), Howard Liver (SRR826795, SRR826796, SRR826797), Huh Linter (SRR5227294, SRR5227295, SRR5227296, SRR5227303, SRR5227304, SRR5227305), Jan Yeast (SRR1562907, SRR1562909, SRR1562911, SRR1562913), Kidney Castelo (all 24 RP samples, GSE81283), 3-AT Yeast (SRR1042865, SRR1042866, SRR1042867).

Acknowledgments

We thank Nicolas Bonhoure and Stefan Morgenthaler for useful discussions. Research in the Naef laboratory was supported by the EPFL. Some computations were performed on the Vital-It computing platform.

Conflict of interest statement

EM, FG, CG and BW were employees of Nestle Institute of Health Sciences SA, CH-1015 Lausanne, Switzerland.

Supplementary material

Table 1. Inferred codon-specific DTs

Table 2. Inferred inter-site codon pair DTs

Table 3. Ribosome profiling in AL and FA mice w/o CHX

Table 4. (aminoacyl-) tRNA profiling in AL and FA mice

References

- Gobet, C. & Naef, F. Ribosome profiling and dynamic regulation of translation in mammals. *Current Opinion in Genetics and Development* **43**. ISSN: 18790380. doi:10.1016/j.gde.2017.03.005 (2017).
- Hinnebusch, A. G. & Lorsch, J. R. The mechanism of eukaryotic translation initiation: new insights and challenges. *Cold Spring Harbor perspectives in biology* **4**, a011544. ISSN: 1943-0264 (Oct. 2012).
- Brule, C. E. & Grayhack, E. J. Synonymous Codons: Choose Wisely for Expression. *Trends in Genetics* **33**, 283–297. ISSN: 01689525 (Apr. 2017).

- 635 4. Presnyak, V. *et al.* Codon Optimality Is a Major Determinant of mRNA Stability. *Cell*
636 **160**, 1111–1124. ISSN: 00928674 (Mar. 2015).
- 637 5. Radhakrishnan, A. *et al.* The DEAD-Box Protein Dhh1p Couples mRNA Decay and Trans-
638 lation by Monitoring Codon Optimality. *Cell* **0**, 1497–1506. ISSN: 00928674 (2016).
- 639 6. Pelechano, V., Wei, W. & Steinmetz, L. M. Widespread co-translational RNA decay reveals
640 ribosome dynamics. *Cell*. ISSN: 10974172. doi:10.1016/j.cell.2015.05.008 (2015).
- 641 7. Yu, C. H. *et al.* Codon Usage Influences the Local Rate of Translation Elongation to
642 Regulate Co-translational Protein Folding. *Molecular Cell* **59**, 744–754. ISSN: 10974164
643 (2015).
- 644 8. Chu, D., Kazana, E., Bellanger, N., Singh, T., Tuite, M. F. & Von Der Haar, T. Translation
645 elongation can control translation initiation on eukaryotic mRNAs. *EMBO Journal* **33**, 21–
646 34. ISSN: 02614189 (2014).
- 647 9. Goodarzi, H., Nguyen, H. C., Zhang, S., Dill, B. D., Molina, H. & Tavazoie, S. F. Modulated
648 Expression of Specific tRNAs Drives Gene Expression and Cancer Progression. *Cell* **165**,
649 1416–1427. ISSN: 00928674 (June 2016).
- 650 10. Loayza-Puch, F. *et al.* Tumour-specific proline vulnerability uncovered by differential ribo-
651 some codon reading. *Nature* **530**, 490–494. ISSN: 0028-0836 (Feb. 2016).
- 652 11. Rapino, F. *et al.* Codon-specific translation reprogramming promotes resistance to targeted
653 therapy. *Nature* **558**, 605–609. ISSN: 14764687 (2018).
- 654 12. Varenne, S., Buc, J., Lloubes, R. & Lazdunski, C. Translation is a non-uniform process.
655 *Journal of Molecular Biology* **180**, 549–576. ISSN: 00222836 (Dec. 1984).
- 656 13. Quax, T. E., Claassens, N. J., Söll, D. & van der Oost, J. Codon Bias as a Means to
657 Fine-Tune Gene Expression. *Molecular Cell* **59**, 149–161. ISSN: 10972765 (July 2015).

14. Sørensen, M. A. & Pedersen, S. Absolute in vivo translation rates of individual codons in *Escherichia coli*. The two glutamic acid codons GAA and GAG are translated with a threefold difference in rate. *Journal of Molecular Biology* **222**, 265–280. ISSN: 00222836 (1991).
15. Ingolia, N. T., Lareau, L. F. & Weissman, J. S. Ribosome Profiling of Mouse Embryonic Stem Cells Reveals the Complexity and Dynamics of Mammalian Proteomes. *Cell* **147**, 789–802. ISSN: 00928674 (Nov. 2011).
16. Ingolia, N. T. Ribosome Footprint Profiling of Translation throughout the Genome. *Cell* **165**, 22–33. ISSN: 00928674 (Mar. 2016).
17. Charneski, C. A. & Hurst, L. D. Positively charged residues are the major determinants of ribosomal velocity. *PLoS biology* **11**, e1001508. ISSN: 1545-7885 (2013).
18. Darnell, A. M., Subramaniam, A. R. & O'Shea, E. K. Translational Control through Differential Ribosome Pausing during Amino Acid Limitation in Mammalian Cells. *Molecular Cell* **71**, 229–243. ISSN: 10974164 (2018).
19. Saikia, M., Wang, X., Mao, Y., Wan, J., Pan, T. & Qian, S.-B. Codon optimality controls differential mRNA translation during amino acid starvation. doi:10.1261/rna.058180.116.
20. Gydosh, N. R. & Green, R. Dom34 Rescues Ribosomes in 3 Untranslated Regions. *Cell* **156**, 950–962 (2014).
21. Nedialkova, D. D. & Leidel, S. A. Optimization of Codon Translation Rates via tRNA Modifications Maintains Proteome Integrity. *Cell* **161**, 1606–1618. ISSN: 00928674 (June 2015).
22. Tuorto, F. *et al.* The tRNA methyltransferase Dnmt2 is required for accurate polypeptide synthesis during haematopoiesis. *The EMBO Journal* **34**, 2350–2362 (2015).

- 682 23. Chou, H. J., Donnard, E., Gustafsson, H. T., Garber, M. & Rando, O. J. Transcriptome-
683 wide Analysis of Roles for tRNA Modifications in Translational Regulation. *Molecular Cell*
684 **68**, 978–992. ISSN: 10974164 (2017).
- 685 24. Pop, C. *et al.* Causal signals between codon bias , mRNA structure , and the efficiency of
686 translation and elongation. *Molecular systems biology*, 1–16 (2014).
- 687 25. Zhang, S., Hu, H., Zhou, J., He, X., Jiang, T. & Zeng, J. Analysis of Ribosome Stalling
688 and Translation Elongation Dynamics by Deep Learning. *Cell Systems* **5**, 212–220. ISSN:
689 24054720 (Sept. 2017).
- 690 26. Döring, K. *et al.* Profiling Ssb-Nascent Chain Interactions Reveals Principles of Hsp70-
691 Assisted Folding. *Cell* **170**, 298–311. ISSN: 10974172 (2017).
- 692 27. Harigaya, Y. & Parker, R. The link between adjacent codon pairs and mRNA stability.
693 *BMC Genomics*. ISSN: 14712164. doi:10.1186/s12864-017-3749-8 (2017).
- 694 28. Gamble, C. E., Brule, C. E., Dean, K. M., Fields, S. & Grayhack, E. J. Adjacent Codons
695 Act in Concert to Modulate Translation Efficiency in Yeast. *Cell*. ISSN: 10974172. doi:10.
696 1016/j.cell.2016.05.070 (2016).
- 697 29. Dao Duc, K. & Song, Y. S. The impact of ribosomal interference, codon usage, and exit
698 tunnel interactions on translation elongation rate variation. *PLoS Genetics*. ISSN: 15537404.
699 doi:10.1371/journal.pgen.1007166 (2018).
- 700 30. O'Connor, P. B. F., Andreev, D. E. & Baranov, P. V. Comparative survey of the relative
701 impact of mRNA features on local ribosome profiling read density. *Nature Communications*
702 **7**, 12915. ISSN: 2041-1723 (Oct. 2016).
- 703 31. Gardin, J., Yeasmin, R., Yurovsky, A., Cai, Y., Skiena, S. & Fletcher, B. Measurement of
704 average decoding rates of the 61 sense codons in vivo. *eLife*. ISSN: 2050084X. doi:10.7554/
705 eLife.03735 (2014).

32. Aeschimann, F., Xiong, J., Arnold, A., Dieterich, C. & Großhans, H. Transcriptome-wide measurement of ribosomal occupancy by ribosome profiling. *Methods*. ISSN: 10959130. doi:10.1016/j.ymeth.2015.06.013 (2015).
33. Lareau, L. F., Hite, D. H., Hogan, G. J. & Brown, P. O. Distinct stages of the translation elongation cycle revealed by sequencing ribosome-protected mRNA fragments. *eLife*. ISSN: 2050084X. doi:10.7554/eLife.01257 (2014).
34. Duncan, C. D. S. & Mata, J. Effects of cycloheximide on the interpretation of ribosome profiling experiments in *Schizosaccharomyces pombe*. *Scientific Reports*. ISSN: 2045-2322. doi:10.1038/s41598-017-10650-1 (2017).
35. Gerashchenko, M. V., Lobanov, A. V. & Gladyshev, V. N. Genome-wide ribosome profiling reveals complex translational regulation in response to oxidative stress. *Proceedings of the National Academy of Sciences* **109**, 17394–17399. ISSN: 0027-8424 (Oct. 2012).
36. Hussmann, J. a., Patchett, S., Johnson, A., Sawyer, S. & Press, W. H. Understanding Biases in Ribosome Profiling Experiments Reveals Signatures of Translation Dynamics in Yeast. *PLOS Genetics* **11** (ed Snyder, M.) e1005732. ISSN: 1553-7404 (Dec. 2015).
37. Tunney, R., McGlincy, N. J., Graham, M. E., Naddaf, N., Pachter, L. & Lareau, L. F. Accurate design of translational output by a neural network model of ribosome distribution. *Nature Structural and Molecular Biology* **25**, 577–582. ISSN: 15459985 (2018).
38. Quax, T. E., Claassens, N. J., Söll, D. & van der Oost, J. Codon Bias as a Means to Fine-Tune Gene Expression. *Molecular Cell* **59**, 149–161. ISSN: 10972765 (July 2015).
39. Orioli, A. tRNA biology in the omics era: Stress signalling dynamics and cancer progression. *BioEssays*. ISSN: 15211878. doi:10.1002/bies.201600158 (2017).
40. Huter, P. *et al.* Structural Basis for Polyproline-Mediated Ribosome Stalling and Rescue by the Translation Elongation Factor EF-P. *Molecular Cell*. ISSN: 10974164. doi:10.1016/j.molcel.2017.10.014 (2017).

41. Woolstenhulme, C. J., Guydosh, N. R., Green, R. & Buskirk, A. R. High-Precision analysis of translational pausing by ribosome profiling in bacteria lacking EFP. *Cell Reports* **11**, 13–21. ISSN: 22111247 (2015).
42. Pelechano, V. & Alepuz, P. EIF5A facilitates translation termination globally and promotes the elongation of many non polyproline-specific tripeptide sequences. *Nucleic Acids Research* **45**, 7326–7338. ISSN: 13624962 (2017).
43. Lubas, M. *et al.* eIF5A is required for autophagy by mediating ATG3 translation. doi:10.15252/embr.201846072.
44. Hinnebusch, A. G., Ivanov, I. P. & Sonenberg, N. Translational control by 5'-untranslated regions of eukaryotic mRNAs. *Science* **352**, 1413–1416. ISSN: 0036-8075 (June 2016).
45. Jan, C. H., Williams, C. C. & Weissman, J. S. Principles of ER cotranslational translocation revealed by proximity-specific ribosome profiling. *Science* **346**, 1257521–1257521. ISSN: 0036-8075 (Nov. 2014).
46. Gerashchenko, M. V. & Gladyshev, V. N. Translation inhibitors cause abnormalities in ribosome profiling experiments. *Nucleic Acids Research*. ISSN: 13624962. doi:10.1093/nar/gku671 (2014).
47. Zhang, F., Xu, X., Zhou, B., He, Z. & Zhai, Q. Gene Expression Profile Change and Associated Physiological and Pathological Effects in Mouse Liver Induced by Fasting and Refeeding. *PLoS ONE* **6** (ed Androulakis, I. P.) e27553. ISSN: 1932-6203 (Nov. 2011).
48. Howard, M. T., Carlson, B. a., Anderson, C. B. & Hatfield, D. L. Translational redefinition of UGA codons is regulated by selenium availability. *Journal of Biological Chemistry* **288**, 19401–19413. ISSN: 00219258 (2013).
49. Castelo-Szekely, V., Arpat, A. B., Janich, P. & Gatfield, D. Translational contributions to tissue specificity in rhythmic and constitutive gene expression. *Genome Biology* **18**. ISSN: 1474760X. doi:10.1186/s13059-017-1222-2 (2017).

50. Lintner, N. G. *et al.* Selective stalling of human translation through small-molecule engagement of the ribosome nascent chain. *PLoS Biology*. ISSN: 15457885. doi:10.1371/journal.pbio.2001882 (2017).
51. Dittmar, K. A., Sørensen, M. A., Elf, J., Ehrenberg, M. & Pan, T. Selective charging of tRNA isoacceptors induced by amino-acid starvation. *EMBO Reports*. ISSN: 1469221X. doi:10.1038/sj.embor.7400341 (2005).
52. Canella, D. *et al.* A multiplicity of factors contributes to selective RNA polymerase III occupancy of a subset of RNA polymerase III genes in mouse liver. *Genome Research*. ISSN: 10889051. doi:10.1101/gr.130286.111 (2012).
53. Rudolph, K. L. M. *et al.* Codon-Driven Translational Efficiency Is Stable across Diverse Mammalian Cell States. *PLoS Genetics* **12**, 1–23. ISSN: 15537404 (2016).
54. Pechmann, S. & Frydman, J. Evolutionary conservation of codon optimality reveals hidden signatures of cotranslational folding. *Nature Structural and Molecular Biology*. ISSN: 15459993. doi:10.1038/nsmb.2466 (2013).
55. Chevance, F. F. V. & Hughes, K. T. Case for the genetic code as a triplet of triplets. *Proceedings of the National Academy of Sciences*. ISSN: 0027-8424. doi:10.1073/pnas.1614896114 (2017).
56. Kanaya, S., Yamada, Y., Kudo, Y. & Ikemura, T. Studies of codon usage and tRNA genes of 18 unicellular organisms and quantification of *Bacillus subtilis* tRNAs: Gene expression level and species-specific diversity of codon usage based on multivariate analysis. *Gene*. ISSN: 03781119. doi:10.1016/S0378-1119(99)00225-5 (1999).
57. Ingolia, N. T. Ribosome profiling: new views of translation, from single codons to genome scale. *Nature Reviews Genetics* **15**, 205–213. ISSN: 1471-0056 (Mar. 2014).

- 779 58. Mohammad, F., Woolstenhulme, C. J., Green, R. & Buskirk, A. R. Clarifying the Trans-
780 lational Pausing Landscape in Bacteria by Ribosome Profiling. *Cell Reports* **14**, 686–694.
781 ISSN: 22111247 (Feb. 2016).
- 782 59. Wu, C. C.-C., Zinshteyn, B., Wehner, K. A. & Green, R. High-Resolution Ribosome Pro-
783 filing Defines Discrete Ribosome Elongation States and Translational Regulation during
784 Cellular Stress. *Molecular Cell* **0**, 1–12. ISSN: 10972765 (Jan. 2019).
- 785 60. Rodnina, M. V. The ribosome in action: Tuning of translational efficiency and protein
786 folding. *Protein Science* **25**, 1390–1406. ISSN: 09618368 (Aug. 2016).
- 787 61. Agris, P. F., Eruysal, E. R., Narendran, A., Väre, V. Y. P., Vangaveti, S. & Ranganathan,
788 S. V. Celebrating Wobble Decoding: Half a century and still much is new. *RNA Biology*.
789 ISSN: 1547-6286. doi:10.1080/15476286.2017.1356562 (2017).
- 790 62. Alkatib, S. *et al.* The Contributions of Wobbling and Superwobbling to the Reading of
791 the Genetic Code. *PLoS Genetics*. ISSN: 15537390. doi:10.1371/journal.pgen.1003076
792 (2012).
- 793 63. Yang, J. R., Chen, X. & Zhang, J. Codon-by-Codon Modulation of Translational Speed
794 and Accuracy Via mRNA Folding. *PLoS Biology*. ISSN: 15457885. doi:10.1371/journal.
795 pbio.1001910 (2014).
- 796 64. Stadler, M. & Fire, A. Wobble base-pairing slows in vivo translation elongation in meta-
797 zoans. *RNA* **17**, 2063–2073. ISSN: 1355-8382 (Dec. 2011).
- 798 65. Pavlov, M. Y., Watts, R. E., Tan, Z., Cornish, V. W., Ehrenberg, M. & Forster, A. C. Slow
799 peptide bond formation by proline and other N-alkylamino acids in translation. *Proceedings*
800 *of the National Academy of Sciences* **106**, 50–54. ISSN: 0027-8424 (2009).
- 801 66. Fujimura, K., Choi, S., Wyse, M., Strnadel, J., Wright, T. & Klemke, R. Eukaryotic trans-
802 lation initiation factor 5A (EIF5A) regulates pancreatic cancer metastasis by modulating

RhoA and rho-associated kinase (ROCK) protein expression levels. *Journal of Biological Chemistry*. ISSN: 1083351X. doi:10.1074/jbc.M115.687418 (2015).

67. Mandal, A., Mandal, S. & Park, M. H. Global quantitative proteomics reveal up-regulation of endoplasmic reticulum stress response proteins upon depletion of eIF5A in HeLa cells. *Scientific Reports*. ISSN: 20452322. doi:10.1038/srep25795 (2016).

68. Shek, F. H., Fatima, S. & Lee, N. P. Implications of the Use of Eukaryotic Translation Initiation Factor 5A (eIF5A) for Prognosis and Treatment of Hepatocellular Carcinoma. *International Journal of Hepatology* **2012**. doi:10.1155/2012/760928 (2012).

69. Shalgi, R., Hurt, J. A., Krykbaeva, I., Taipale, M., Lindquist, S. & Burge, C. B. Widespread Regulation of Translation by Elongation Pausing in Heat Shock. *Molecular Cell* **49**, 439–452. ISSN: 10972765 (Feb. 2013).

70. Fang, H., Huang, Y. F., Radhakrishnan, A., Siepel, A., Lyon, G. J. & Schatz, M. C. Scikit-ribo Enables Accurate Estimation and Robust Modeling of Translation Dynamics at Codon Resolution. *Cell Systems*. ISSN: 24054720. doi:10.1016/j.cels.2017.12.007 (2018).

71. Somogyi, P., Jenner, A. J., Brierley, I. & Inglis, S. C. Ribosomal pausing during translation of an RNA pseudoknot. *Molecular and cellular biology* **13**, 6931–40. ISSN: 0270-7306 (1993).

72. Tholstrup, J., Oddershede, L. B. & Sørensen, M. A. mRNA pseudoknot structures can act as ribosomal roadblocks. *Nucleic Acids Research*. ISSN: 03051048. doi:10.1093/nar/gkr686 (2012).

73. Dittmar, K. A., Goodenbour, J. M. & Pan, T. Tissue-specific differences in human transfer RNA expression. *PLoS genetics* **2**, e221. ISSN: 1553-7404 (Dec. 2006).

74. Tatarinova, T. V., Alexandrov, N. N., Bouck, J. B. & Feldmann, K. A. GC3biology in corn, rice, sorghum and other grasses. *BMC Genomics* **11**. ISSN: 14712164. doi:10.1186/1471-2164-11-308 (2010).

- 827 75. Wolfson, R. L. & Sabatini, D. M. The Dawn of the Age of Amino Acid Sensors for the
828 mTORC1 Pathway. *Cell Metabolism* **26**, 301–309. ISSN: 19327420 (Aug. 2017).
- 829 76. Zheng, G. *et al.* Efficient and quantitative high-throughput tRNA sequencing. *Nature meth-*
830 *ods* **12**, 835–837. ISSN: 1548-7105 (Sept. 2015).
- 831 77. Dobin, A. *et al.* STAR: Ultrafast universal RNA-seq aligner. *Bioinformatics* **29**, 15–21.
832 ISSN: 13674803 (2013).
- 833 78. Robinson, M. D., McCarthy, D. J. & Smyth, G. K. edgeR: a Bioconductor package for
834 differential expression analysis of digital gene expression data. *BIOINFORMATICS AP-*
835 *PLICATIONS NOTE* **26**, 139–140 (2010).
- 836 79. Atger, F. *et al.* Circadian and feeding rhythms differentially affect rhythmic mRNA tran-
837 scription and translation in mouse liver. *Proceedings of the National Academy of Sciences*
838 **112**, E6579–E6588. ISSN: 0027-8424 (Nov. 2015).
- 839 80. Lowe, T. M. & Chan, P. P. tRNAscan-SE On-line: integrating search and context for
840 analysis of transfer RNA genes. *Nucleic acids research*. ISSN: 13624962. doi:10.1093/nar/
841 gkw413 (2016).

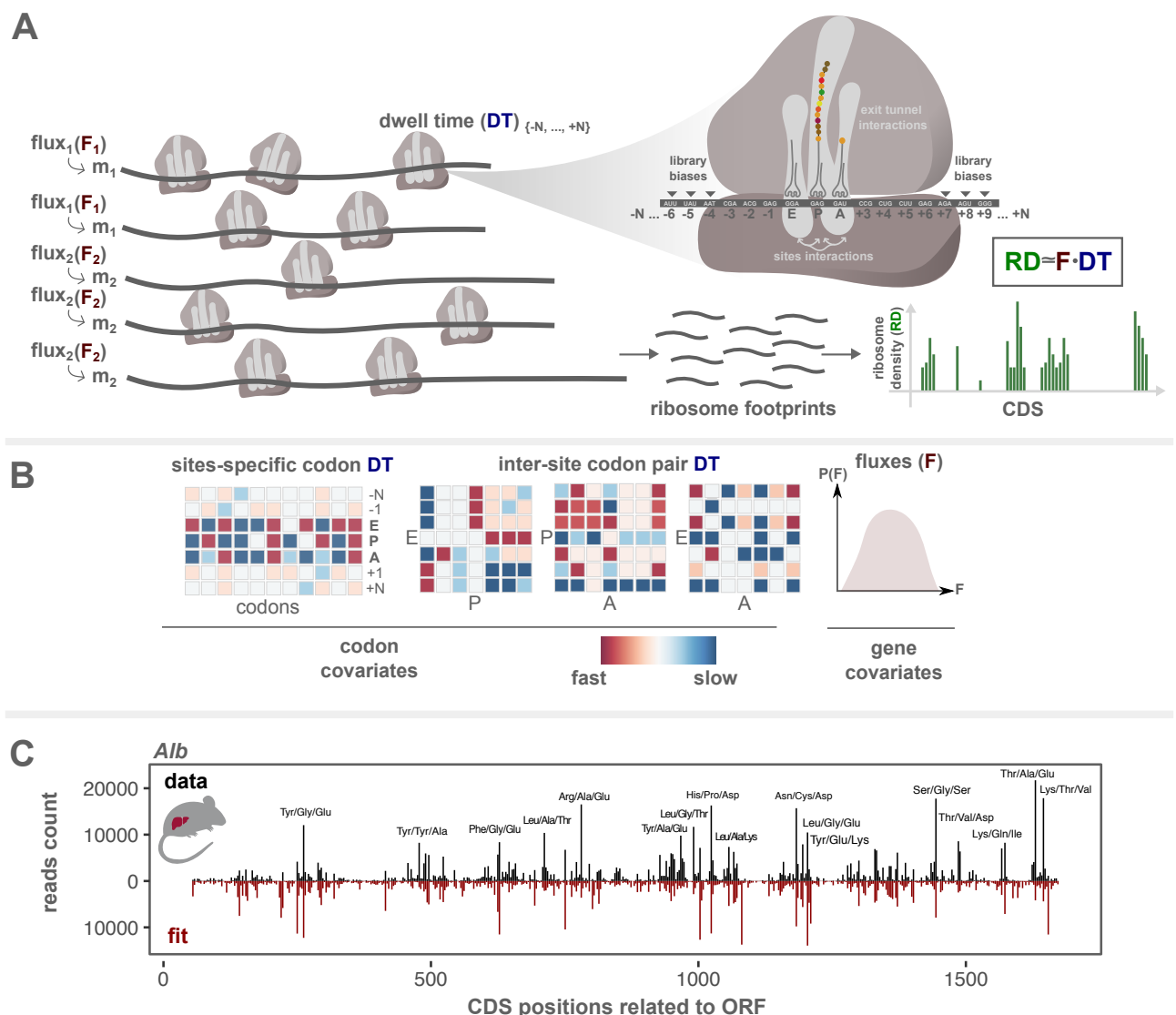


Figure 1: Modeling ribosome fluxes and codon-specific DT including ribosome inter-site interactions

A. Ribosome elongation: Snapshot of two different mRNA species (m_1, m_2) translated with two different fluxes (F_1, F_2). Zoomed ribosome shows that numerous factors regulate ribosome DTs: 40 codons (+20,-20) around the E site are taken into account in the model to alleviate possible library biases, exit tunnel interactions, and influence of upstream/downstream sequences. Codon-pair interactions between the three sites (E, P, A) are also modeled. The ribosome densities on the mRNAs are estimated by RP, and modeled as genes fluxes multiplied by DTs. B. Site- and codon- specific DTs are visualized in a heatmap, relative to the position mean. The matrix of inter-sites interactions (E:P, P:A and E:A) shows all possible combinations of codon pairs. All regression coefficients (gene fluxes and DTs) are inferred genome-wide. C. Observed (black) and predicted (red) read counts for *Albumin* in mouse liver. Peaks with a high number of reads (long DTs) are annotated with their respective AA in the E, P, and A sites.

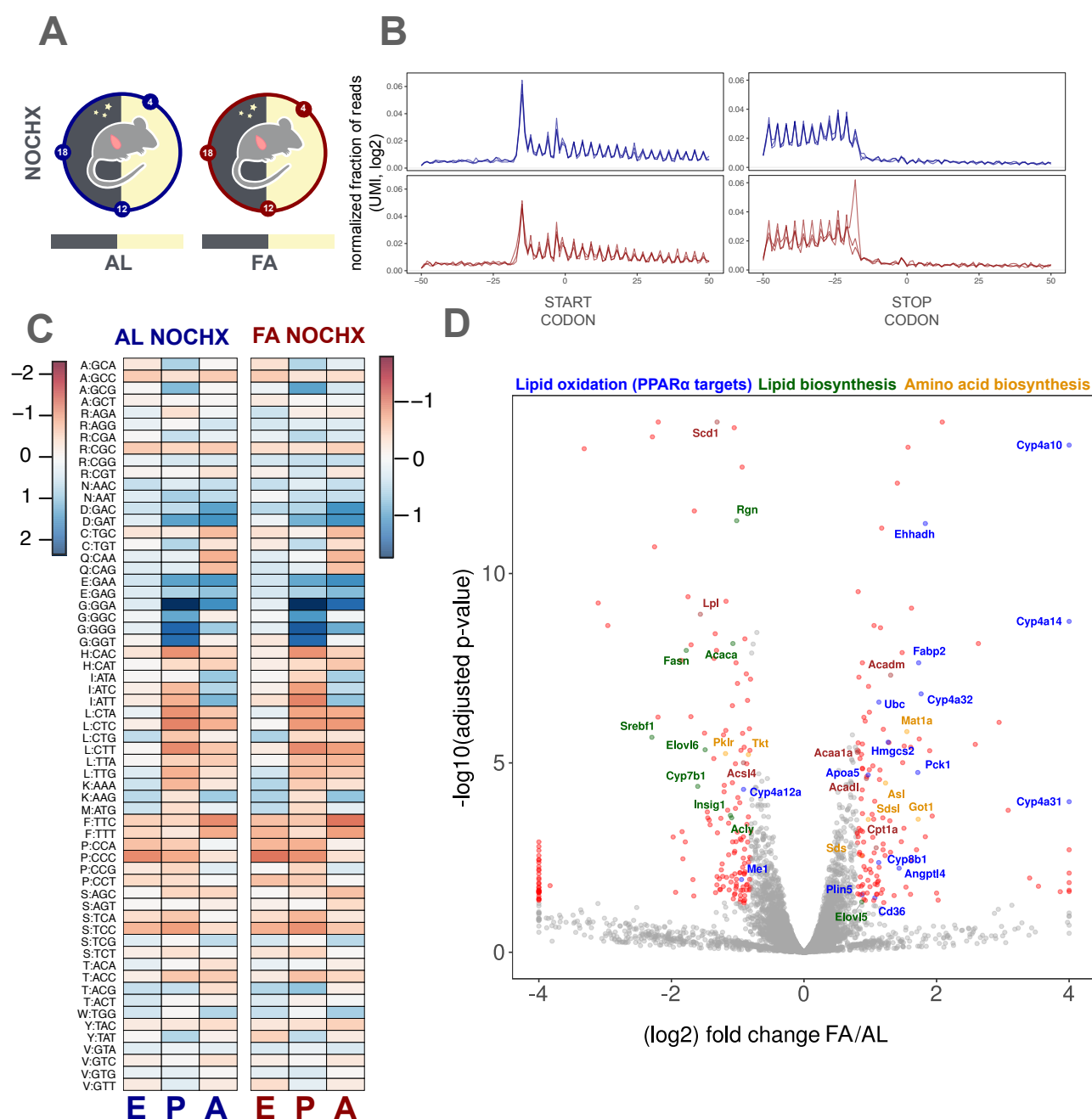


Figure 4: Ribosome DTs are not affected in fasted mice and without CHX

Individual DTs are retrieved from the fit with the P:A interaction. A. Livers from mice fed AL or FA were harvested at ZT04, ZT12, and ZT18. RP was performed without CHX in the lysis buffer. B. Normalized fractions of reads of length 32 around the start and stop codons in a window of 100 nucleotides genome-wide. Dark blue: AL/NOCHX; dark red: FA/NOCHX. C. DTs (log2, mean centered per site, heatmap) for the E, P, and A sites in AL/NOCHX and FA/NOCHX. Codons are ordered by AA. Side bars: log2 color scale. D. Differential expression of RP signals between AL and FA (Methods). Benjamini-Hochberg adjusted p-values ($-\log_{10}$) plotted against averaged log2 fold change between FA and AL. Genes with FDR < 1% and absolute log2 fold change > 1 are annotated and colored. Blue: genes in the KEGG "PPAR α signal pathway"; Green: KEGG and GO term "lipid biosynthesis"; Orange: KEGG "AA biosynthesis".

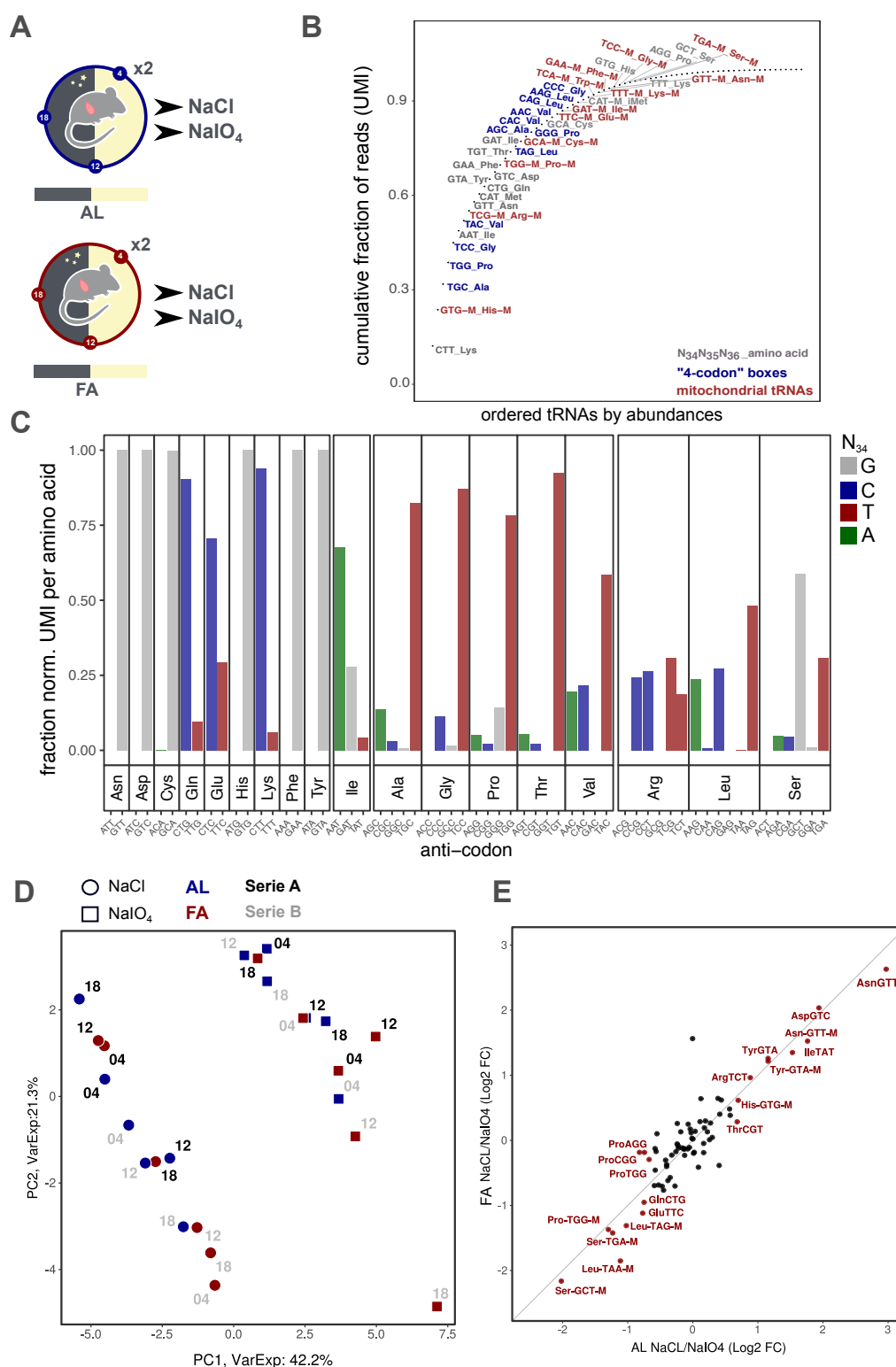


Figure 5: (Aminoacyl-) tRNA profiling in AL fed and FA mice

A. Mice fed AL or FA were sacrificed at ZT04 (fasting duration: 16 h), ZT12 (24 h) and ZT18 (30 h) and livers were harvested. Each sample was treated with NaCl and sodium periodate (NaIO₄). B. Cumulative fraction of reads for each tRNA, ordered by abundances. Anticodons and AAs are indicated for the 50 first codons. Blue: four-codon box AA; red: mitochondrial tRNAs. C. Fraction of reads (UMI) per AA for the different isoacceptor tRNAs. Colors indicate the nucleotide in position 34 on the tRNA. D. PCA of the tRNA abundances (log2 UMI). PC1 and PC2 explain 42.2% and 21.3% of the variance, respectively, and separate NaCl from NaIO₄ treatment. NaCl (circle), NaIO₄ (square), AL (blue), FA (red), replicate 1 (black), replicate 2 (grey). ZT is shown beside the points. E. Ratio of tRNA abundances (log2 fold change, averaged over the time points) between the NaCl and NaIO₄ for AL fed vs. FA mice (significant changes, $p < 0.05$ in red). No tRNA showed a significant difference between AL and FA (*i.e.* fell out of the diagonal).

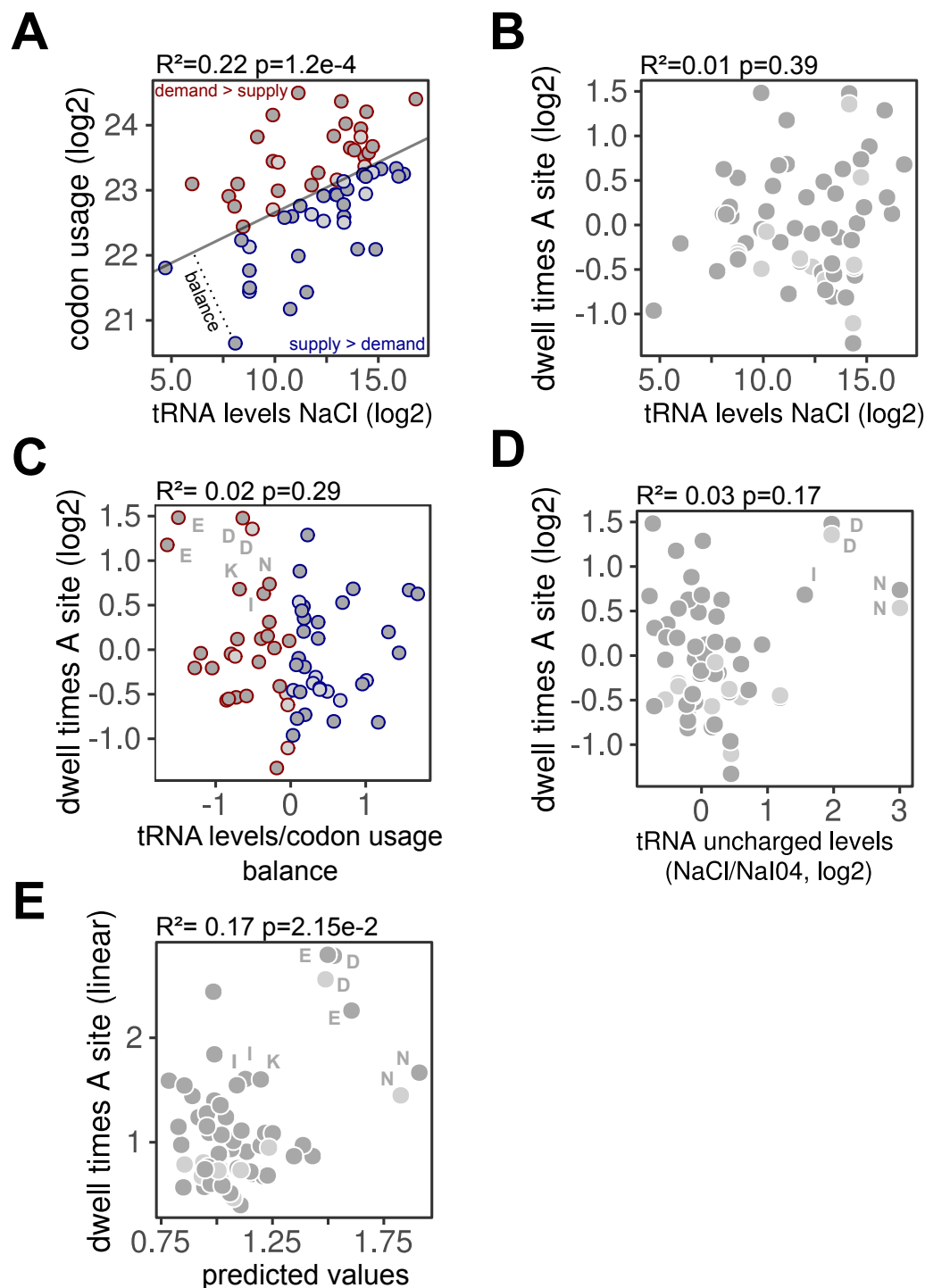


Figure 6: Relationship between (aminoacyl-) tRNA levels, codon usage and DT

A. Significant correlation ($R^2 = 0.22, p = 1.2e - 4$) between wCU frequency (log2) and normalized total tRNA (NaCl) read count for each codon (log2, UMI, averaged over the AL samples). The gray line shows the first principal component (PC). Orthogonal distance to the PC reflects the balance between tRNA supply and demand. Codons with positive (resp. negative) balance are colored blue (resp. red). Codons are assigned to their canonical tRNAs (dark-grey) or to wobble tRNAs (light-grey) where appropriate (Methods). B. DTs in the A site (log2) vs. tRNA levels (NaCl, log2) averaged over the AL samples ($R^2 = 0.01, p = 3.9e - 1$). C. Correlation between tRNA levels/codon usage balance and DT in the A site (log2) averaged over the AL samples. R^2 and p-value are reported for the linear regression ($R^2 = 0.02, p = 2.9e - 1$). D. Correlation between tRNA uncharged levels (NaCl/NaIO₄, log2) and DTs in the A site (log2) averaged over the AL samples. R^2 and p-value are reported for the linear regression ($R^2 = 0.03, p - value = 1.7e - 1$). Positively correlated codons are annotated by their one-letter AA. E. Significant correlation ($R^2 = 0.17, p - value = 2.15e - 02$) between estimated and predicted DTs in the A site. Prediction uses a linear model with the balance and uncharged levels, in linear scale, as explanatory variables. In C-E, annotations refer to one-letter AA.

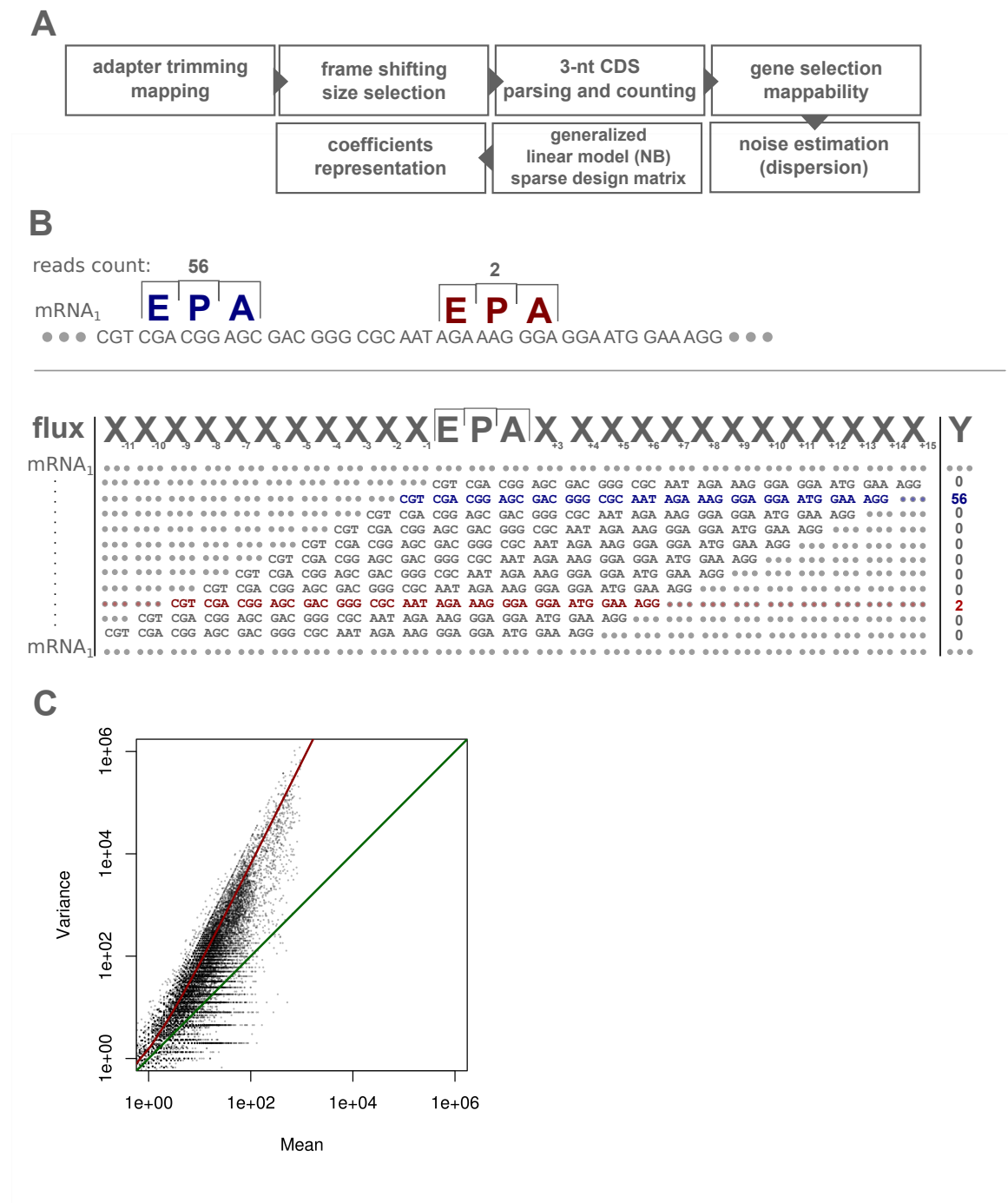


Figure S1: **Bioinformatics pipeline, RP count, and noise model**

A. Bioinformatics pipeline: Sequencing reads are trimmed and mapped to the genome. Reads are first selected based on their size and P sites are assigned for each read. All annotated CDSs are parsed with a step of 3 nucleotides and number of reads are reported at each position. Genes with insufficient total read counts and read densities are removed, as well as regions with non-unique mappability. Dispersion parameters for negative binomial distributions are estimated for each sample and the GLM is fitted with a sparse design matrix and negative binomial (NB) noise model. DTs are centered (in log2 scale) and represented as shown in Fig. 1 B. B. Construction of the data matrix for the GLM. Example of a gene CDS with two different positions (dark blue and dark red) covered by 56 and 2 reads, respectively. The assigned E, P, and A sites are shown. The CDS is parsed 3-by-3 and a matrix is designed with the corresponding position-dependent codons. C. Mean and variance of measured counts for pairs of codons occurring multiple times on a gene. The green line shows a *Poisson* regime with the variance equal to the mean. The red line represents the estimated fit for a negative binomial distribution (Methods). The dispersion parameter is estimated from these fits and used to parameterize the NB used in the GLM, independently for each sample.

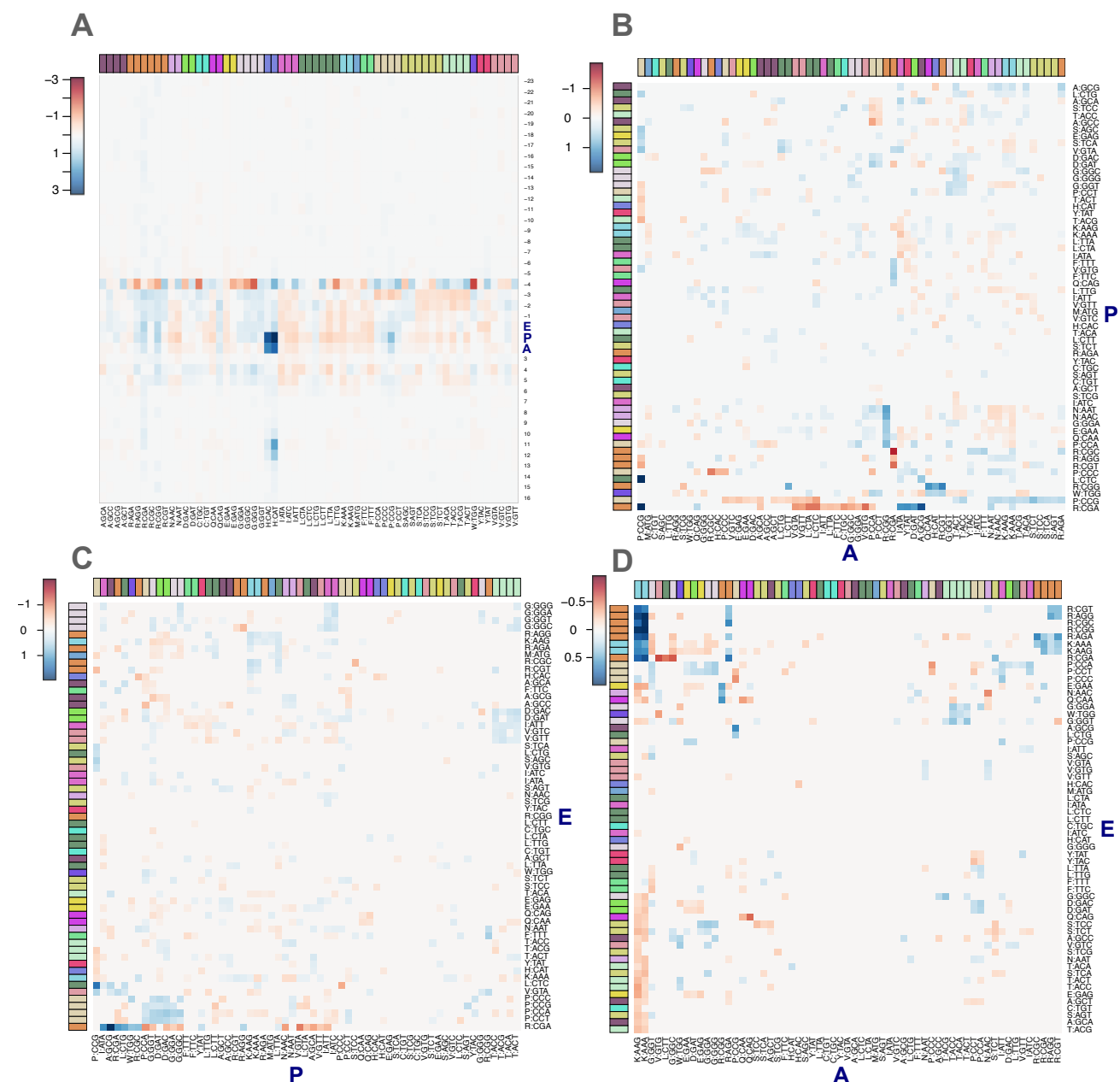


Figure S2: In yeast ribosome DT anticorrelate with codon usage and display site interactions

Panels for the site-specific DTs are retrieved from the fit with the P:A interaction. A. Heatmap representation of the DTs (log2, mean centered per site) in a window of 40 codons around the E site. Codons are ordered by AA and colored accordingly at the top of the heatmap. DTs with $p \geq 0.05$ are not shown (set to zero). B. Interaction matrix for the pairs P:A (log2). Codons are colored according to AA. Codons in both sites are hierarchically clustered based on the euclidean distance matrix and a complete linkage algorithm. Fast and slow interactions are shown respectively in dark red and dark blue (colorbar). DTs with p -value ≥ 0.05 are set to zero. C. Same as (B) for the pairs E:P. D. Same as (B) for the pairs E:A.

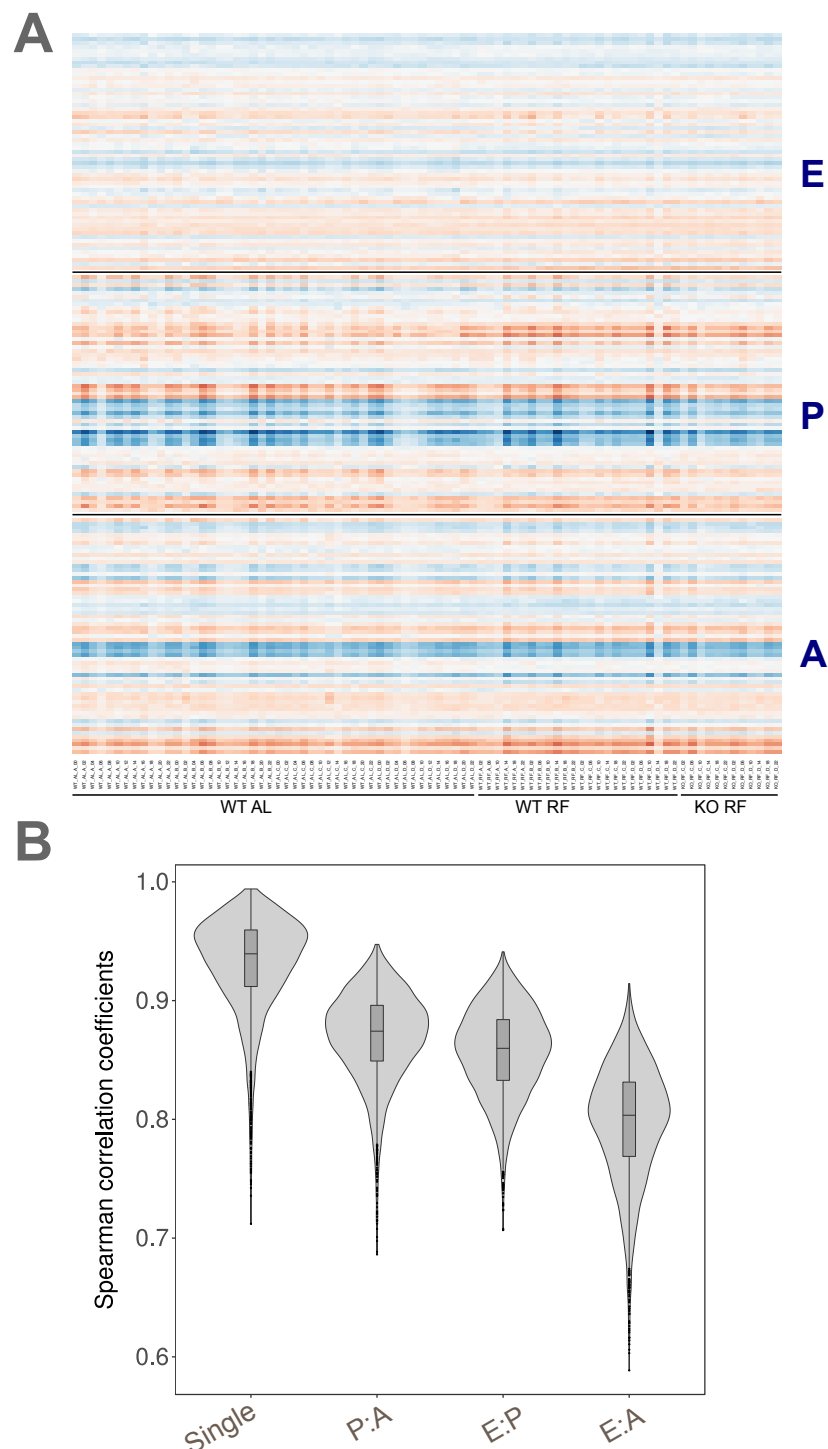


Figure S3: Sample specific DTs and correlations

A. DTs (log2, mean centered per site) at the E, P, and A sites for the 84 samples in the three conditions WT AL (WT ad libitum), WT RF (WT night-restricted feeding) and KO RF (*Bmal1* KO night-restricted feeding).
 B. Inter-sample Spearman correlation coefficients for site-specific DTs (single) and inter-site codon DTs for the interactions P:A, E:P, and E:A.

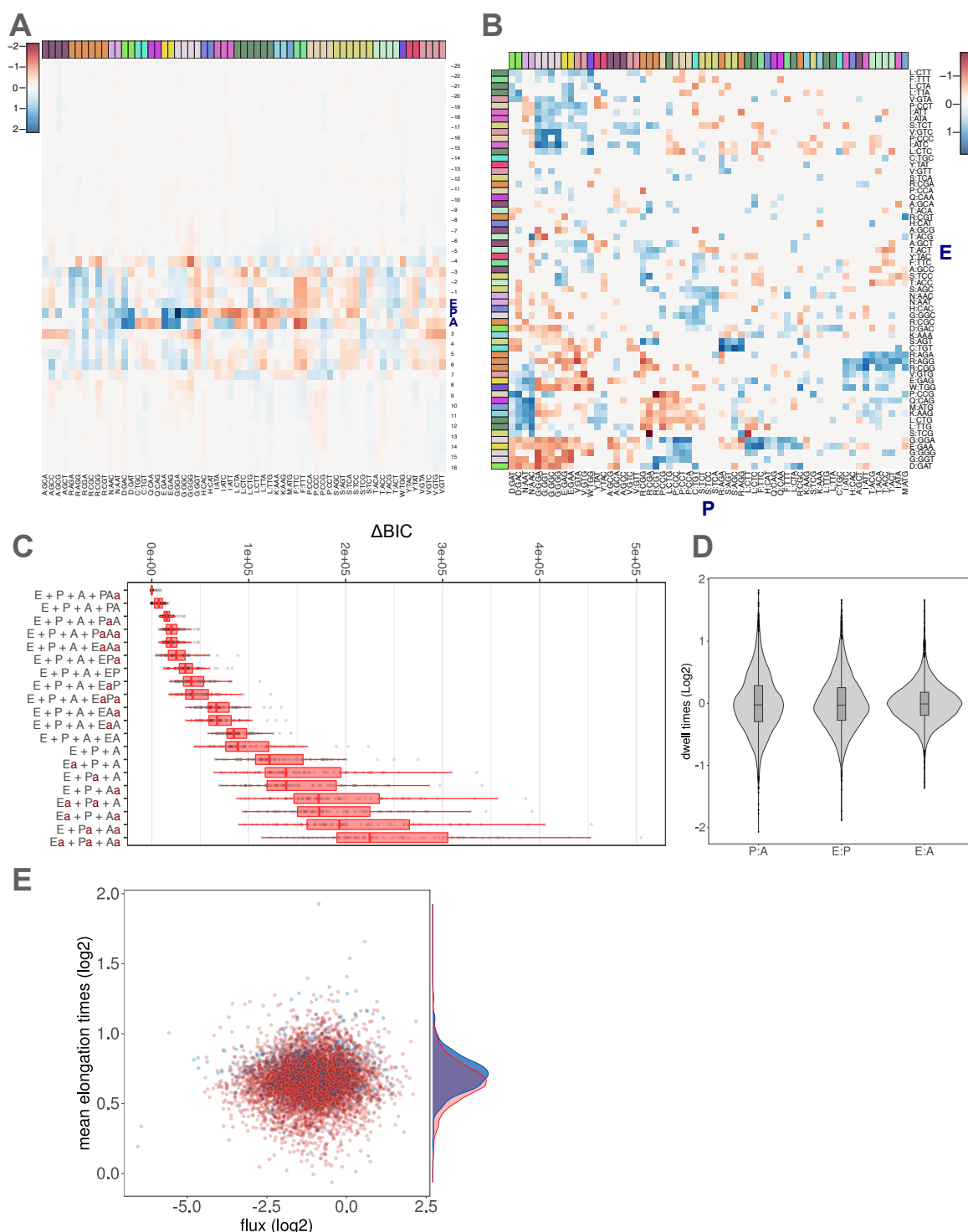


Figure S4: Extended analysis of the translation elongation landscape in mouse liver

Site-specific DTs are retrieved from the fit with the P:A interaction. A. Heatmap representation of the DTs (log2, mean centered per site) in a window of 40 codons around the E site. Codons are ordered by AA and colored accordingly. DTs with $p \geq 0.05$ are not shown (set to zero). B. Interaction matrix for E:P pairs(log2). Codons are colored according to AA. Codons in both sites are hierarchically clustered based on the euclidean distance matrix and a complete linkage algorithm. Relatively fast and slow interactions are shown respectively in dark red and dark blue. DTs with p -value ≥ 0.05 are not shown (set to zero). C. Differences of Bayesian Information Criterion (ΔBIC) between the model shown and the best model. (ΔBIC) is computed for each sample and proposed model, in which the alphabet for the DT covariates was taken as either the 20 natural AA or the 61 sense codons. A lowercase 'a' on the right of an uppercase letter indicates that the AA alphabet was used for this position. D. DT (log2) distributions and boxplots for the three interaction terms P:A, E:P and E:A of the 84 samples in mouse liver. E. Translation fluxes (log2) averaged across the 84 samples vs. the mean gene elongation time (computed as the log2 DTs (P + A + PA), summed in lear scale over the gene CDS and divided by the respective CDS length). Genes related to the gene ontology term "cytoskeleton" are colored in blue. Marginal distributions are plotted on the side.

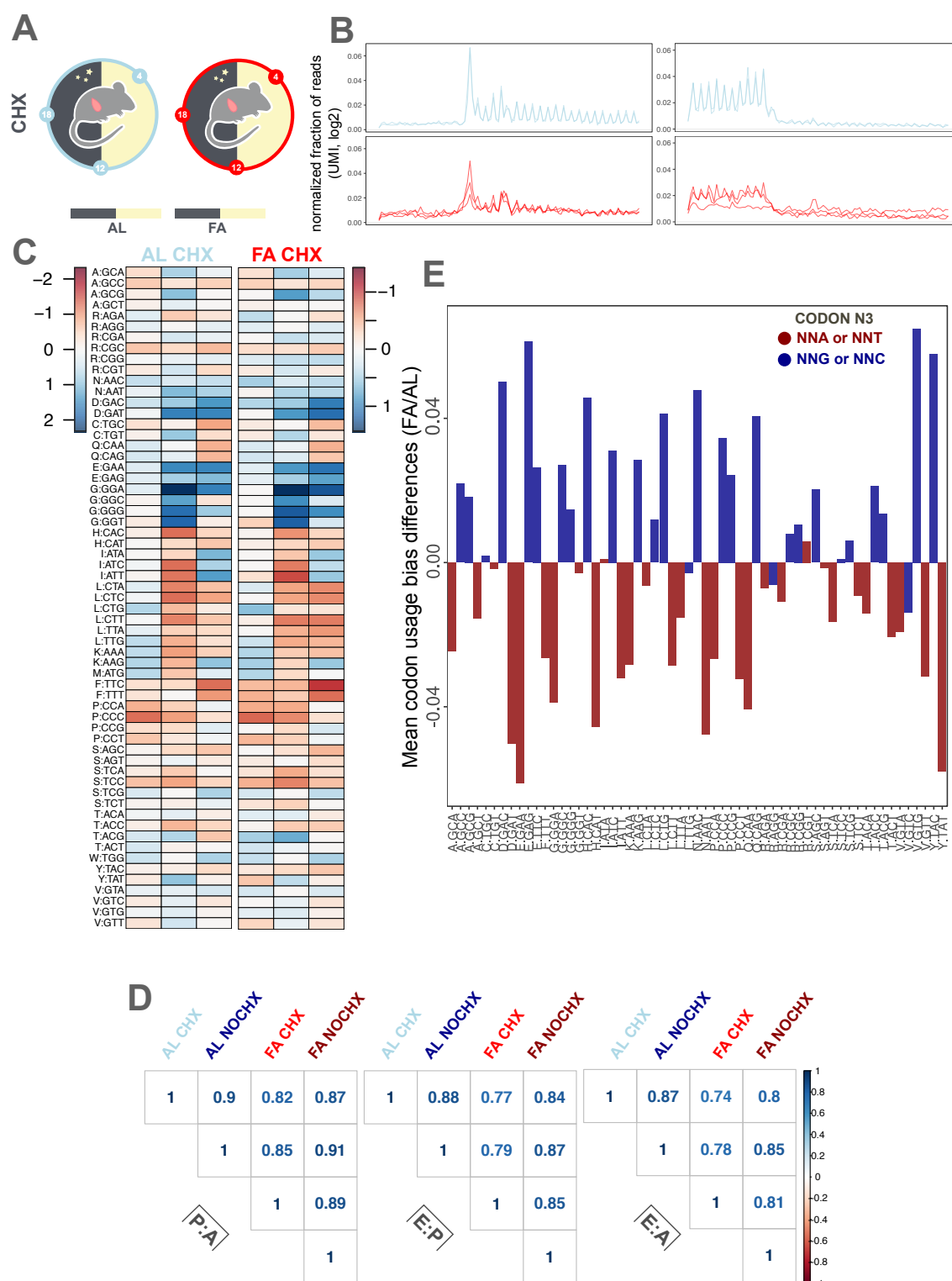


Figure S5: **Ribosome DTs are not affected in fasted mice and with CHX**

A. Liver from mice fed (AL) or fasted (FA) were harvested at ZT04, ZT12, and ZT18. RP was performed with CHX in the lysis buffer. B. Pileup plots representing normalized fractions of reads of length 32 around the start and stop codons in a window of 100 nucleotides across all selected genes. Each sample is depicted with a color corresponding to one of the four conditions (light blue AL/CHX, light red FA/CHX). C. Heatmap representation of the DTs (log₂, mean centered per site) for the E, P, and A sites in AL/CHX and FA/CHX conditions. Codons are ordered by the respective AA. log₂ color scale is shown on the side each heatmap. D. Pearson correlation coefficient (R) between the different conditions for the interaction terms (log₂) E:P, P:A, and E:A. E. Codon usage bias is computed for each gene up- or down-regulated in fasted animals and averaged. The difference in codon usage bias is computed between the FA and AL conditions. Codons are colored accordingly to their nucleotide at the third position (G-C in blue and A-T in red).

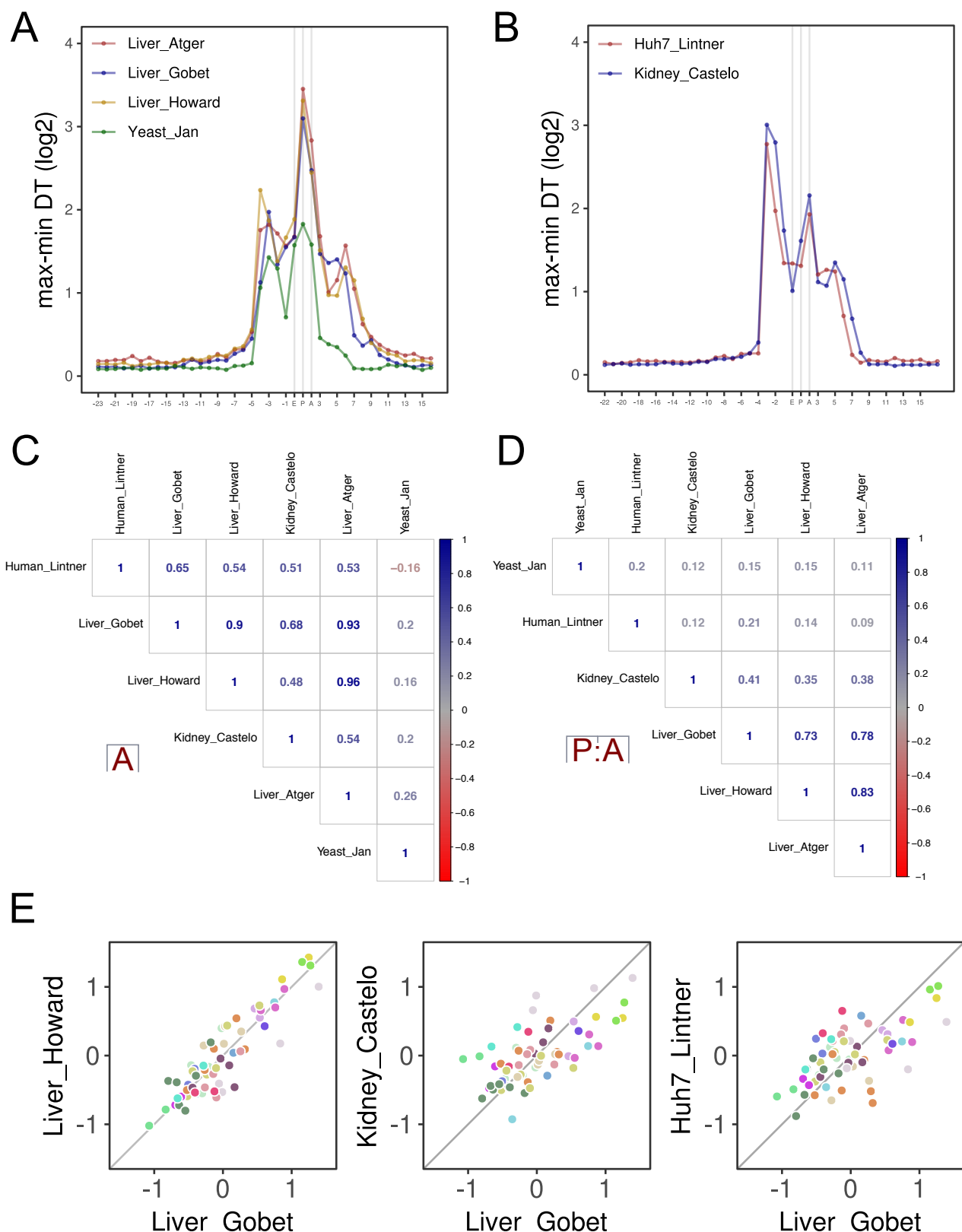


Figure S6: Meta-analysis revealed conserved DT patterns and technical biases

Analysis of published RP datasets in yeast (Yeast Jan) [45], mouse liver (Liver Atger, Liver Howard, Liver Gobet (this paper)) [79, 48], mouse kidney (Kidney Castelo) [49] and in a human hepatocyte cell line (Huh7 Lintner) [50]. DTs were inferred for each sample and averaged by condition. A. Spread of the DTs (max-min, log2) at every positions in a window of 40 codons around the E site for studies using small RNA library protocols. Colors show the different datasets. B. Same as (A) for studies using "circularization" library protocols. C. Correlation for the A site DTs between the different datasets (Pearson coefficient is color coded). D. Same as (C) for P:A interaction. E. DTs in the A site for the Liver Howard, Kidney Castelo and Huh7 Lintner datasets vs. DTs in the A site from the RP data in this paper (Liver Gobet, AL and FA).

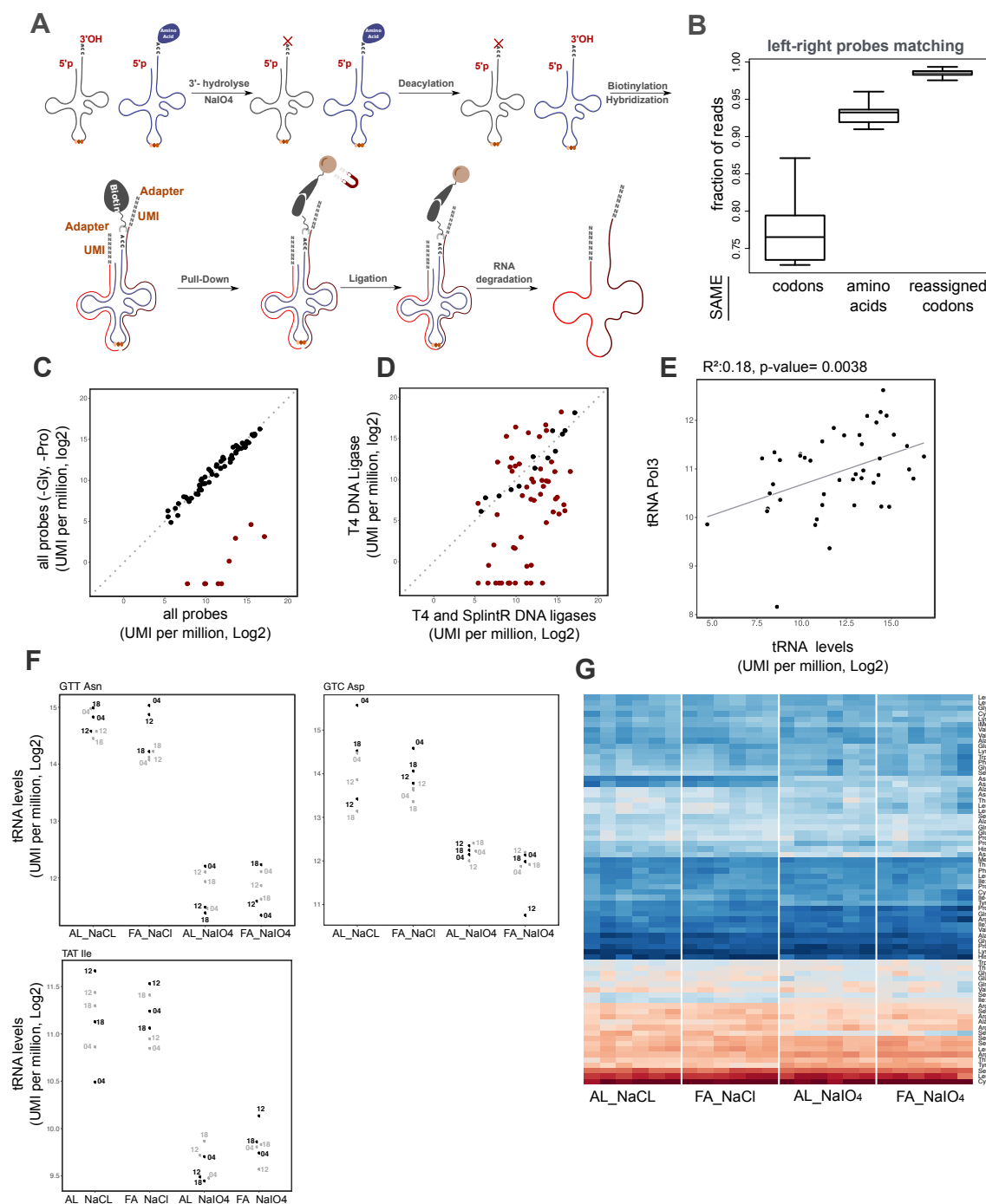


Figure S7: (aminoacyl-) tRNA profiling in AL fed and FA mice (bis)

A. tRNA profiling protocol. tRNAs were extracted in acidic conditions and uncharged tRNAs were hydrolyzed at 3'-end upon periodate treatment. tRNAs were treated with NaCl in control conditions. Then, tRNAs were deacylated and biotinylated at their 3'-end. Mix of left and right DNA probes were hybridized to the tRNA pools and pulled-down on magnetic beads through biotin-streptavidin interactions. Nicks in the anticodon between the left and right probes were ligated. tRNAs were degraded and DNA probes sequenced after amplification. B. Reads were mapped on every combination of left and right probes. Fraction of reads corresponding to left-right probe combinations belonging to the same codon or AA is reported for the 24 samples. The same measure is computed after reassignment of the probe combinations (Methods). C. tRNA abundances (log2) at the codon level for the control vs. altered conditions in which probes related to tRNAs coding for Pro and Gly were removed. D. tRNA abundances (log2) at the codon level for experiments with T4 or SplintR DNA ligases. Significant differences are shown in red. E. Correlation between tRNA abundances in control AL vs. RNA polymerase III (POL3) ChIP-Seq signal quantified on the tRNAs gene loci. Data were extracted from the supplementary table of ref. [52]. F. Expression levels for three tRNA coding respectively for Asn, Asp, and Ile, showing 5-8 fold differences between control and periodate-treated conditions. G. Heatmaps of the normalized tRNA read count (log2 UMI per million) at the codon level for the 24 samples. tRNAs are ordered with hierarchical clustering. Dark blue (high), dark red (low).